Improving the Regulation Range of EV Battery Chargers With *L3C2* Resonant Converters

Navid Shafiei, *Student Member, IEEE*, and Martin Ordonez, *Member, IEEE*

***Abstract*—The demand for electric vehicles has expanded rapidly for both industrial and transportation applications. In parallel, new battery technologies capable of deeply discharging and powering electric vehicles over long periods of time have been introduced and made available in the market. Due to the increasing complexity of charging algorithms, battery chargers are exposed to demanding operating requirements. Chargers should not only work under different loading conditions (from absolutely zero to maximum output power) but also regulate a wide output voltage range (from near zero to 1.5 times nominal voltage). In this paper, a multiresonant $L3C2$ resonant converter is introduced that can cover nearly all of the regions in the battery *V–I* plane, from near zero output voltage, zero output current to maximum output power. By adding one capacitor, the topology is able to extend the operating frequency beyond the LLC topology and achieve significant regulation improvements. Near free-ripple charging current for batteries charging is achieved in different states of charge without using burst mode operation, effectively increasing the battery life cycle. In addition, soft transitions are obtained for all the switches (MOSFETs and diodes) resulting in high efficiency, reliability, power density, and low-noise operation of the charger. A complete set of simulation and experimental results, extracted from a 96-VDC 950-W $L3C2$ resonant converter, demonstrates the characteristic features of the proposed topology for battery charger applications, while providing a comparative example with the LLC topology.**

***Index Terms*—Battery charger, full soft switching conditions, multiresonant *L3C2* resonant converter, recovering dead battery, wide output voltage regulation.**

NOMENCLATURE

C_j	Diode junction capacitance (F).
C_n	Resonant capacitance ratio $(C_n = C_t/C_s)$.
C_p	Parallel resonant capacitance (F).
C_s	Series-resonant capacitance (F).
C_t	Equivalent parallel resonant capacitance (F).
$C_{w,s}$	Winding capacitance of the transformer secondary side (F).
f_0	Series-resonant frequency (Hz).
$f_{r,\text{oc1}}$	First open-circuit resonant frequency (Hz).
$f_{r,\text{oc2}}$	Second open-circuit resonant frequency (Hz).
$f_{r,\text{sc}}$	Short-circuit resonant frequency (Hz).
f_s	Switching frequency (Hz).
$I_{L_{s_1}}$	Peak current of the first series-resonant inductance (A).
$I_{L_{s_2}}$	Peak current of the second series-resonant inductance (A).
I_{out}	DC output current (A).
L_{ext}	External series inductance (H).
$L_{lk,p}$	Transformer primary leakage inductance (H).
$L_{lk,s}$	Transformer secondary leakage inductance (H).
L_m	Transformer magnetizing inductance (H).
L_n	Resonant inductance ratio $(L_n = L_{s1}/L_p)$.
L_p	Parallel resonant inductance (H).
L_s	Series-resonant inductance ratio $(L_s = L_{s1}/L_{s2})$.
L_{s_1}	First series-resonant inductance (H).
L_{s_2}	Second series-resonant inductance (H).
M_{V_r}	AC–AC voltage transfer function of the *LLC* resonant inverter.
M_{V_R}	AC–DC voltage transfer function of the current driven rectifier.
M_{V_s}	DC–AC voltage transfer function of the half-bridge inverter.
n	Transformer turns-ratio $(n = N_p/N_s)$.
Q_L	Loaded quality factor.
R_L	Load resistance (Ω).
V_1	Fundamental component of the half-bridge output voltage.
V_{in}	DC input voltage (V).
V_{out}	DC output voltage (V).
$V_{\text{out},m,NL}$	Minimum dc output voltage in no-load condition (V).
$V_{\text{out},n}$	Nominal dc output voltage (V).
$V_{R_{\text{eq}}}$	Output voltage amplitude of the *LLC* resonant inverter.
Z_0	Series characteristic impedance (Ω).

I. INTRODUCTION

IN the past decade, the use of electric vehicles (EVs) has increased rapidly, creating a tangible alternative to offset greenhouse gas emissions. EVs are propelled by electric motors, which are powered by rechargeable batteries. With the development of high-power rechargeable batteries, work that encompasses the full design and implementation of smart battery chargers for EVs has gained attention [1]. There are different types of rechargeable battery packs in the market (Li-Ion, lead-acid, NiMH, etc.) which are used as power sources in EVs [2]–[5]. Using batteries for energy storage imposes challenging design constraints for chargers, due to the different operating modes of the battery, including constant current, constant voltage, constant power, no-load condition, and revitalization. The

Manuscript received January 19, 2014; revised June 13, 2014; accepted June 23, 2014. Date of publication July 9, 2014; date of current version January 16, 2015. This work was supported by the Natural Sciences and Engineering Research Council, Canada. Recommended for publication by Associate Editor M. Ferdowsi.

The authors are with the Department of Electrical and Computer Engineering, The University of British Columbia, Vancouver, BC V6T 1Z4, Canada (e-mail: navid@ece.ubc.ca; mordonez@ieee.org).

Color versions of one or more of the figures in this paper are available online at http://ieeexplore.ieee.org.

Digital Object Identifier 10.1109/TPEL.2014.2336668

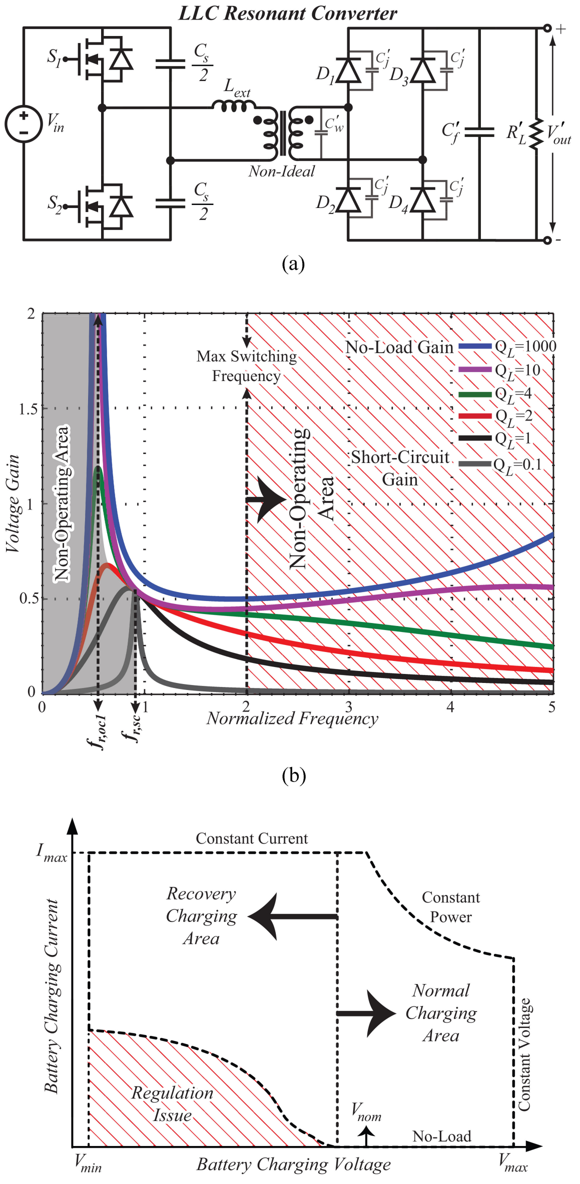

(a)

(b)

(c)

Fig. 1. *LLC* resonant topology: (a) *LLC* schematic including parasitic capacitances, (b) *LLC* voltage gain issues (high frequency) due to the rectifier junction capacitances, and (c) *LLCV–I* plane highlighting regulation issues.

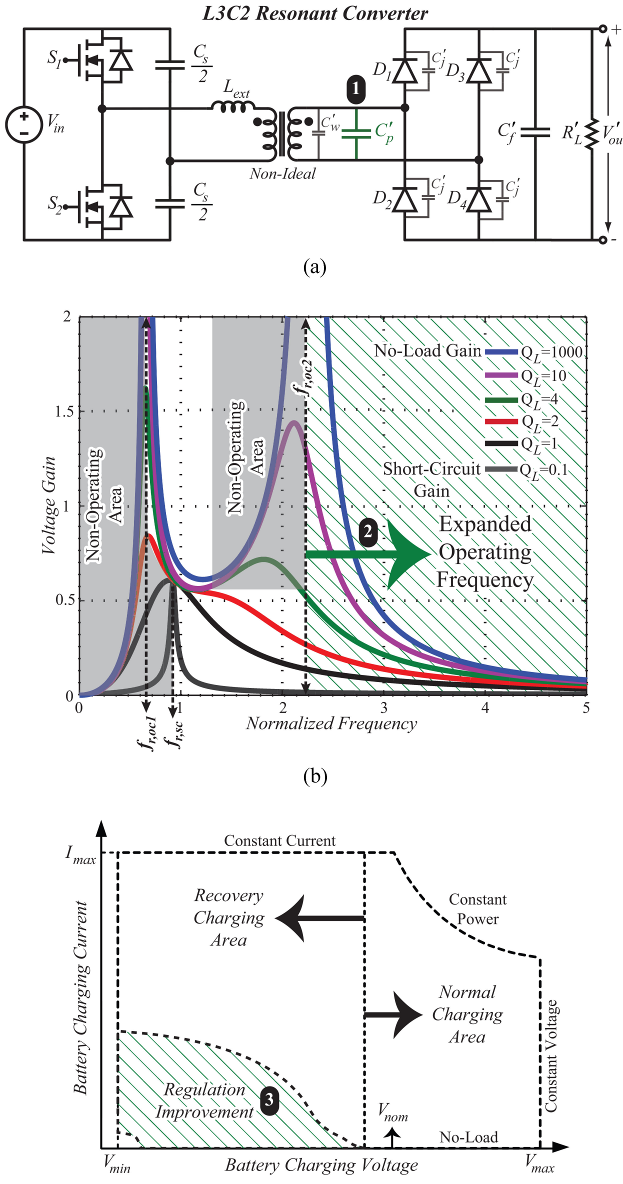

(a)

(b)

(c)

Fig. 2. Proposed $L3C2$ resonant topology solution: (a) $L3C2$ schematic with parallel resonant capacitor in the transformer secondary side ①, (b) $L3C2$ voltage gains with expanded switching frequency operation ②, and (c) $L3C2$ *V–I* plane coverage showing significant regulation improvement ③.

battery charger should not only work in different load conditions, from absolutely zero to maximum output current, but also regulate the output voltage from near zero up to 1.5 times the nominal voltage [6], [7]. The most difficult charging cycle occurs when the battery pack has been discharged completely because of either overdischarging or extended storage time. In this situation, the voltage of the battery pack drops down into dead-zone region, near zero volts per cell. Recently, battery chargers have been designed to revitalize batteries by using a discontinuous charging mode called burst mode. Generally, the burst mode control strategy is employed in light and no-load conditions to improve the regulation and efficiency. In this control method, the switching driver signals are turned ON and OFF periodically at an intermittent cycle much lower than the main switching frequency. In the case of revitalizing a dead battery, the battery absorbs current and the output filter, which is designed for switching frequency, cannot absorb current ripple of the burst mode cycle. As a result, operating the battery charger in this mode leads to low-quality output voltage, and the battery pack is charged with a burst frequency current ripple that can reduce battery life span [7]–[10].

Recently, different studies have been dedicated to developing reliable and efficient battery chargers for EVs. Among power converter topologies, considerations on phase shift full bridge (PSFB) power converter and resonant power converters (e.g., *LLC*) have attracted more attention, and the main reported concerns have been ensuring soft-switching operation, rectifier voltage peak reduction, and extension of the output voltage regulation. The conventional PSFB can regulate the output voltage widely by increasing the phase shift between two legs, but PSFB loses the zero voltage switching (ZVS) in light loads and wide output voltage regulation [6], [11], [12]. Several approaches for the PSFB, including symmetric passive auxiliary circuit, hybrid converters, fixed-variable duty cycle, and self-sustained oscillating control, have been studied in order to extend the output voltage regulation, while provide soft switching condition for semiconductor elements [6], [13]–[15]. However, extreme regulation, which is essential for battery recovery has not been studied yet for PSFB. Voltage peak across the output rectifier diodes is another problem encountered by the conventional PSFB converter, and as a result, diodes with more larger blocking voltage should be selected which leads to more conduction losses and lower efficiency. Different techniques such as *LC* circuits, *RCD* networks, and active rectifiers have been presented for the PSFB in order to eliminate the voltage peak across the output rectifier diodes, but resolving the negative impact on the efficiency and reducing the number of active and passive circuits still remain as research opportunities. [13], [14], [16]. Generally, soft commutation of the output rectifier leads to better selection of the rectifier diodes in terms of reverse voltage, results in high efficiency, lower EMI, and higher switching frequency operation.

Softly switched resonant converters are also candidates for the design of battery charger, due to their capability to produce variable voltage gains in different operating frequencies [7], [17]–[19]. The *LLC* topology has become a popular resonant converter featuring many advantages such as zero voltage and zero-current switching (ZVZCS), and the absorption of the transformer parasitics (leakage and magnetizing inductances) as resonant elements [20]–[23]. Theoretically, it is possible to decrease the output voltage of the *LLC* resonant converter by increasing the switching frequency. However, the existence of diode junction capacitances creates a limitation in the maximum operating frequency [7]–[9], [24]. Fig. 1 presents the *LLC* resonant converter behavior with consideration to the junction capacitance effect. According to this figure, the junction capacitances lead to an unpredicted and unfortunate increase in the voltage gain. As a result, it is not possible to decrease the output voltage by increasing the switching frequency, and therefore, the regulation is lost for low output voltage (indicated by red-dashed areas in Fig. 1). The regulation issues of the *LLC* topology for battery charging are explained in detail in this study with the objective of changing the resonant strategy to overcome these drawbacks.

In comparison with well-known resonant converters such as *LLC* and *LCC*, higher order resonant converters present more desirable characteristics, such as the ability to absorb parasitic inductances and capacitances of the elements and circuit effectively, employing them as resonant elements. Moreover, the diversity of elements in higher order resonant converters gives designers more freedom in the design procedure [25], [26]. Recently, higher order resonant topologies have been introduced in the literature and employed in different industrial applications, such as in photovoltaic module-integrated maximum power point tracker, space power distribution systems, resonant inverters, high-frequency ac distribution systems, and high-voltage dc power supplies [27]–[32].

This paper proposes a multiresonant $L3C2$ resonant converter for battery charging able to operate in a wide switching frequency to regulate the output voltage from near zero to 1.5 times the nominal output voltage in different output load conditions without employing burst mode operation. Fig. 2 shows the $L3C2$ resonant converter structure along with the voltage gain improvements and the *V–I* plain extended operating range (green dashed area). In comparison with the *LLC* resonant topology, the $L3C2$ resonant circuit employs only one extra passive element, a parallel resonant capacitor put in the secondary side of the transformer (green color capacitor). This parallel resonant capacitor leads to zero current switching (ZCS) of the output rectifier diodes, eliminates the voltage peak produced by the diodes reverse recovery current, and decreases the noise in the output voltage. Also, due to the operating in the inductive load, power MOSFETs in the high-frequency $L3C2$ resonant converter always work in ZVS for different load condition, providing high-efficiency, low-noise output voltage. The differences between *LLC* and $L3C2$ resonant converters are depicted in Fig. 2(a)–(c) and in its caption. In comparison with fourth-order resonant topologies, the $L3C2$ resonant converter takes into account the effects of the primary leakage inductance and the secondary leakage inductance separately, which leads to a more accurate steady-state analysis. Moreover, the magnetizing inductance and the secondary winding capacitance are incorporated in this equivalent circuit. The use of a capacitor as an output filter causes a power transfer interruption from resonant circuit toward output side, which must be taken into account in order to conduct a more accurate analysis.

In this paper, the complete analysis of the $L3C2$ resonant converter with consideration of transformer primary and secondary leakage inductances, transformer secondary winding capacitance, and output rectifier junction capacitances is obtained based on first-harmonic approximation (FHA). A detailed analysis is presented to study and compare the $L3C2$ and *LCC* topology. Using the analytical equations extracted from $L3C2$ and *LLC* resonant circuits, two power converters are designed, simulated, implemented, and compared as a $96\text{-VDC}, 950\text{-W}$ battery charger. The results prove the $L3C2$ resonant converter covers almost all regions in the *V–I* plane and can be employed as a wide voltage regulator for battery charger applications.

II. $L3C2$ RESONANT TOPOLOGY AND STEADY-STATE ANALYSIS

The main problem regarding *LLC* resonant converter for wide output voltage regulation is the diode junction capacitance effect on the voltage gain curves. Fig. 1(a) presents the *LLC* resonant converter schematic with a nonideal transformer. In Fig. 1(b), the normalized voltage gains of the half-bridge *LLC* resonant converter versus frequency have been drawn with consideration to the junction capacitance effect of the output rectifier diodes. According to this figure, the junction capacitances lead to a second resonant frequency in the voltage gains, which is far from the short-circuit resonant frequency ($f_{r,\mathrm{sc}}$). The value of second resonant frequency depends on the equivalent parasitic capacitance in the secondary side of the transformer (including diode junction capacitances, printed circuit board layout, and transformer secondary winding) and cannot be estimated easily. According to the obtained experimental results for the *LLC* resonant converter (see Section VII), the second resonant frequency will take place at around two times of short-circuit resonant frequency. Consequently, beside the capacitive load region (in gray), there is a second nonoperating area for the *LLC* resonant converter as indicated by red-dashed regions. In this case, not only the maximum switching frequency is limited by the power electronics design (particularly in magnetic devices), but also important parasitics such as the diode junction capacitances also limits output voltage regulation. Fig 1(c) illustrates the maximum coverage *V–I* plane of the *LLC* resonant converter, including the normal, and recovery charging area, in continuous conduction mode (CCM) [7]. The red-dashed region in Fig. 1(c) indicates the unobtainable area in the *V–I* plane, where switching frequency restriction leads to the regulation issue for the *LLC* resonant converter. Based on the CCM and burst mode operation control technique (combined variable frequency, 150–450 kHz, fixed on time and fixed frequency variable on time), Musavi *et al.* designed and implemented an *LLC* resonant converter as a lead-acid battery charger [7]. Using burst mode operation leads to low-quality output voltage in terms of ripple, and decreases battery life span. The proposed resonant strategy using an $L3C2$ structure is shown in Fig. 2(a). The proposed multiresonant charger consists of a half-bridge inverter, a resonant circuit (including external inductor, nonideal transformer, and parallel capacitor), and a bridge rectifier with capacitive output filter. The parallel resonant capacitor put in the secondary side of the transformer is significantly higher than parasitic capacitors (gray capacitor, C'_w and C'_j), and therefore, overwhelms them and makes the diodes junction and winding capacitances insignificant. The typical voltage gain curves and *V–I* plane of the half-bridge $L3C2$ resonant converter are presented in Fig. 2(b)–(c), respectively. According to these figures, the existence of the parallel resonant capacitor leads to a second resonant frequency in the voltage gains and, as a result, it is feasible to regulate the output voltage in a wide range, from near zero to more than nominal output voltage, by employing variable frequency control. In the following, the complete set of equations for the steady-state analysis of the $L3C2$ and *LLC* resonant converters is presented to highlight their differences solve the regulation issue. In order to reduce the number of definitions, the same normalized parameters are used for final equations, and nonideal transformer models are employed in the equivalent circuits. Also, half-bridge inverters, split series resonant capacitors, and bridge rectifiers with pure capacitive output filters have been selected for both resonant converters.

A. Multiresonant $L3C2$ Resonant Converter With Nonideal Transformer

Fig. 3 shows a complete schematic of the $L3C2$ resonant converter including relevant parasitics. In this figure, a fourth-order model of the transformer (including primary and secondary leakage inductances, magnetizing inductance, and winding capacitance of the transformer secondary side) has been employed as a model for the nonideal transformer [33], [34]. The junction capacitances of the output rectifier are considered in parallel with diodes. According to Fig. 3, the parallel resonant capacitor in the transformer secondary side can integrate parasitic capacitances into the resonant circuit (green capacitors). As depicted in Fig. 3, secondary leakage and the magnetizing inductances of the transformer are considered L_{s_2} and L_p, respectively. In addition, primary leakage inductance is merged with the external inductor and is part of L_{s_1}. In Fig. 3, all of the elements in the secondary side are defined with an apostrophe, but in all equations, the variables and elements are transferred to the primary side with respect to the transformer turns ratio, and are shown without an apostrophe. Different states of the output rectifier along with C_t and its main waveforms are presented in Fig. 4(a) and (b), respectively. In Fig. 4(a), the C_t is defined as follows:

$$C_t = C_w + C_p + C_j. \tag{1}$$

Since there is no inductor at the output of the converter, in the off-state interval of the output rectifier, C_t is disconnected from the output filter, charged and discharged by $i_{L_{s_2}}$, and v_{C_t} has a semisinusoidal shape. The C_t voltage is clamped to the output voltage level while the output rectifier is on, and power is transferred from the resonant circuit to the output. Due to the semisinusoidal waveform of the diode voltage, the diodes turn ON and OFF at low $\frac{dv}{dt}$, and therefore, the drawback effect of the diode junction capacitance in transient time can be minimized. Also, the existence of parallel resonant capacitor with rectifier input port leads to ZCS of the diodes and reduces the EMI noise [26]. There are four states for the output rectifier in each switching period, and all of them are illustrated in Fig. 4(a). According to Fig. 4(b), the rectifier input current is not purely sinusoidal, and the rectifier input voltage has a semisinusoidal shape. As a result, the output rectifier and load cannot be simply modeled by an equivalent resistor. In [32] and [35], an equivalent circuit has been obtained for the output rectifier in parallel and series-parallel resonant converters with capacitive output filters. In fact, a resistive impedance in series with a capacitive impedance is used to model the circuit in Fig. 4(a). The elements of the equivalent circuit are defined as follows:

$$R_{\mathrm{eq}} = \frac{\sin^2\psi}{\pi C_t \omega_s} \tag{2}$$

$$C_{\mathrm{eq}} = \frac{\pi C_t}{\psi - \sin\psi\cos\psi}. \tag{3}$$

In the above equations, the off-state interval, ψ is called nonconduction mode and is given by

$$\psi = \cos^{-1}\left(\frac{\pi - 2\omega_s R_L C_p}{\pi + 2\omega_s R_L C_p}\right). \tag{4}$$

By using the equivalent circuit of Fig. 4(a), it is possible to employ the FHA technique for analysis of the $L3C2$ resonant circuit. In FHA analysis, it is assumed that power is only transferred from the high-frequency resonant circuit to the load via

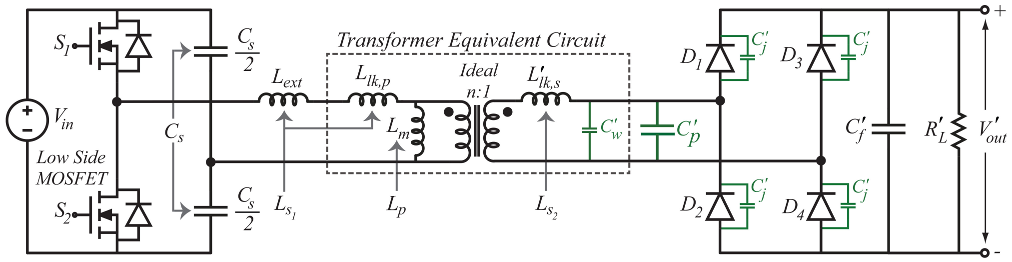

Fig. 3. $L3C2$ resonant converter with nonideal transformer.

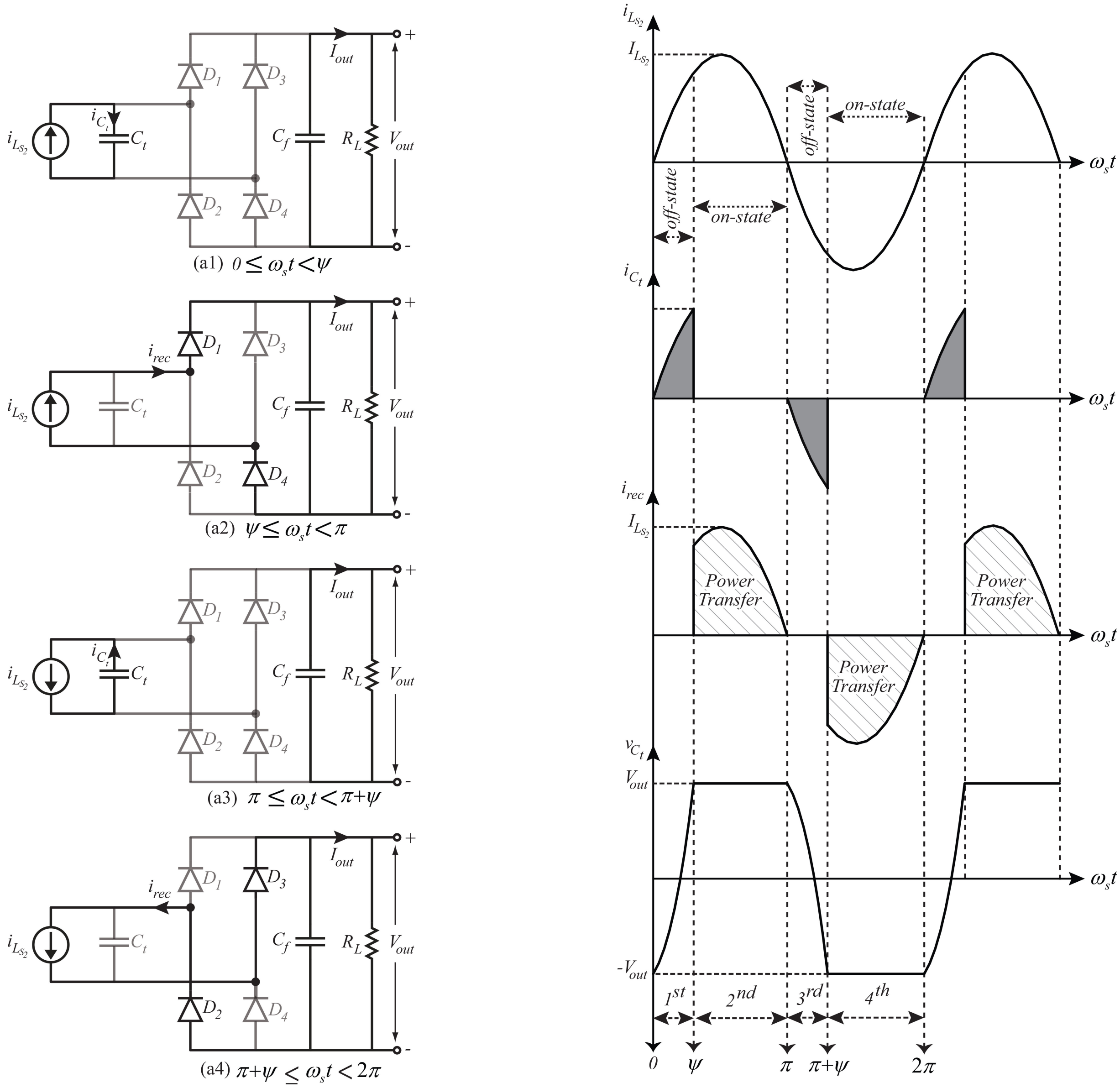

(a)

(b)

Fig. 4. (a) Output rectifier states along with parallel resonant capacitor, and (b) main waveforms of the output rectifier.

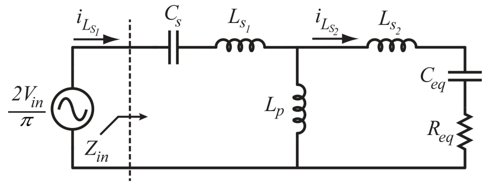

Fig. 5. AC equivalent circuit of the $L3C2$ resonant converter.

the fundamental component. The ac equivalent circuit of the $L3C2$ resonant converter with capacitive output filter is presented in Fig. 5. The output voltage of the half-bridge inverter is a square wave with magnitude of V_{in}. This voltage can be expanded in Fourier series, and the fundamental component can be expressed as follows:

$$v_1 = V_1 \sin(\omega_s t), \quad V_1 = \frac{2V_{\text{in}}}{\pi}. \tag{5}$$

In the following, the ac equivalent circuit is analyzed to extract the steady-state equations of the $L3C2$ resonant converter. In Fig. 5, the input impedance of the resonant circuit is obtained as follows:

$$\begin{aligned}\mathbf{Z}_{\text{in}}(j\omega_s) &= |\mathbf{Z}_{\text{in}}|\, e^{j\varphi} \\ &= \frac{1}{j\omega_s C_s} + j\omega_s L_{s_1} \\ &\quad + (j\omega_s L_p) || \left(j\omega_s L_{s_2} + R_{\text{eq}} + \frac{1}{j\omega_s C_{\text{eq}}} \right).\end{aligned} \tag{6}$$

In the recent equation, φ indicates the phase of the input impedance. Since φ is positive, the resonant circuit represents an inductive load for the half-bridge inverter, and the input current of the resonant circuit $i_{L_{s_1}}$ lags behind the fundamental component of the inverter output voltage. Therefore, ZVS conditions would be provided for power MOSFETs, and the antiparallel diodes turn OFF at low di/dt with no reverse recovery current peak [17]. Operation in this mode is recommended for practical applications. Using the normalized parameters, the normalized input impedance Z_{in}/Z_0 and ψ are derived as follows:

$$\begin{aligned} Q_L &= \frac{R_L}{Z_0}, \quad Z_0 = \sqrt{\frac{L_{s_1}}{C_s}}, \quad \omega_0 = \frac{1}{\sqrt{L_{s_1} C_s}} \\ \omega_n &= \frac{\omega_s}{\omega_0} \end{aligned} \tag{7}$$

$$\begin{aligned}\frac{\mathbf{Z}_{\text{in}}(j\omega_n)}{Z_0} &= \left(j\omega_n + \frac{1}{j\omega_n} \right) \\ &\quad + \frac{\frac{j\omega_n}{L_n} \left(\frac{j\omega_n}{L_s} + \frac{\sin^2\psi}{\pi C_n \omega_n} + \frac{\psi - \sin\psi\cos\psi}{\pi C_n j\omega_n} \right)}{\frac{j\omega_n}{L_n} + \frac{j\omega_n}{L_s} + \frac{\sin^2\psi}{\pi C_n \omega_n} + \frac{\psi - \sin\psi\cos\psi}{\pi C_n j\omega_n}}\end{aligned} \tag{8}$$

$$\psi = \cos^{-1} \frac{\pi - 2C_n Q_L \omega_n}{\pi + 2C_n Q_L \omega_n}. \tag{9}$$

According to Fig. 5 and (5) and (8), the amplitude of $I_{L_{s1}}$ (MOSFETs current) can be obtained as follows:

$$I_{L_{s1}} = \frac{2V_{\text{in}}}{\pi |\mathbf{Z}_{\text{in}}(j\omega_n)|}. \tag{10}$$

In order to calculate the output current, the second resonant inductor current is considered purely sinusoidal with the following equation:

$$i_{L_{s_2}} = I_{L_{s_2}} \sin(\omega_s t + \theta) \tag{11}$$

and as a result, according to Fig. 4, the output current and output voltage are given by

$$\begin{aligned} I_o &= \frac{1}{2\pi} \left(\int_{\psi}^{\pi} i_{L_{s_2}}\, d(\omega_s t) + \int_{\pi+\psi}^{2\pi} i_{L_{s_2}}\, d(\omega_s t) \right) \\ &= \frac{(1+\cos\psi)}{\pi} I_{L_{s_2}} \end{aligned} \tag{12}$$

$$I_{L_{s_2}} = \left| \frac{\frac{j\omega_n}{L_n}}{\frac{j\omega_n}{L_n} + \frac{j\omega_n}{L_s} + \frac{\sin^2\psi}{\pi C_n \omega_n} + \frac{\psi - \sin\psi\cos\psi}{\pi C_n j\omega_n}} \right| I_{L_{s_1}} \tag{13}$$

$$V_{\text{out}} = R_L . I_{\text{out}} = R_L \frac{(1+\cos\psi)}{\pi} I_{L_{s_2}}. \tag{14}$$

The normalized voltage transfer function of the half-bridge $L3C2$ resonant converter with capacitive output filter is calculated as follows:

$$M_v = \frac{V_{\text{out}}}{V_{\text{in}}} = \frac{Q_L Z_0 (1+\cos\psi) I_{L_{s_2}}}{\pi V_{\text{in}}}. \tag{15}$$

Fig. 5 and (8)–(15) can be employed to analyze the steady-state behavior of the $L3C2$ resonant converter with capacitive output filter.

B. LLC Resonant Converter With Nonideal Transformer

Fig. 6(a) presents the *LLC* resonant converter with nonideal transformer. The typical equations for analyzing the *LLC* resonant converter consider the equivalent leakage inductance for the transformer [19]–[21]. In the following, for more accurate analysis, primary and secondary leakage inductances are considered separately for steady-state analysis. The secondary leakage inductance and the magnetizing inductance of the transformer are considered L_{s_2} and L_p, respectively. The primary leakage inductance is absorbed by external inductor and is a part of L_{s_1}. The *LLC* resonant converter is not able to absorb parasitic capacitances, indicated in the secondary side with red color (C'_w and C'_j). The objective of this review is to highlight and clarify the shortcoming of the *LLC* topology for battery charging in the high-frequency range. Unlike the $L3C2$ resonant converter, the analysis for the *LLC* resonant converter is straightforward. In this converter, the power transfer interruption does not occur because the output rectifier is a current driven rectifier and is compatible with the high-frequency *LLC* resonant inverter. As a result, it is possible to model the output rectifier, C-filter, and the load with an equivalent resistor [17]

$$R_{\text{eq}} = \frac{8}{\pi^2} R_L, \quad Q_L = \frac{R_{\text{eq}}}{Z_0}. \tag{16}$$

The ac equivalent circuit of the *LLC* resonant converter is shown in Fig. 6(b). The input voltage of the resonant circuit can be expressed by (5). By considering the ac equivalent circuit and the normalized parameters introduced in (7), the input

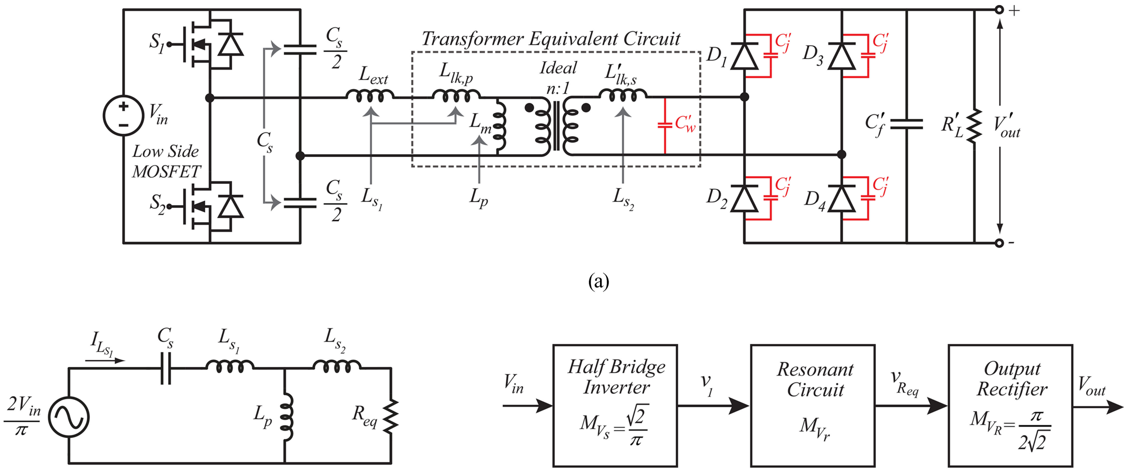

(a)

(b) (c)

Fig. 6. (a) *LLC* resonant converter with nonideal transformer, (b) ac equivalent circuit of the *LLC* resonant converter, and (c) resonant converter block diagram.

impedance is obtained

$$\mathbf{Z}_{\text{in}}(j\omega_s) = |\mathbf{Z}_{\text{in}}|\, e^{j\varphi} = \frac{1}{j\omega_s C_s} + j\omega_s L_{s_1} + (j\omega_s L_p)||(j\omega_s L_{s_2} + R_{\text{eq}}) \tag{17}$$

$$\frac{\mathbf{Z}_{\text{in}}(j\omega_n)}{Z_0} = \left(j\omega_n + \frac{1}{j\omega_n}\right) + \frac{\frac{j\omega_n}{L_n}\left(\frac{j\omega_n}{L_s} + Q_L\right)}{\frac{j\omega_n}{L_n} + \frac{j\omega_n}{L_s} + Q_L}. \tag{18}$$

In order to obtain the voltage transfer function, it is necessary to calculate the voltage gain of each part of the *LLC* resonant converter. In Fig. 6(c), the *LLC* resonant converter block diagram is shown. According to this figure, the resonant converter consists of three parts, namely, the half-bridge inverter, resonant circuit, and output rectifier. As a result, the voltage transfer function is a product of these parts

$$M_v = \frac{V_{\text{out}}}{V_{\text{in}}} = M_{V_s} \,.\, M_{V_r} \,.\, M_{V_R} = \frac{M_{V_r}}{2} \tag{19}$$

$$M_{V_r} = \left|\frac{j\omega_n Q_L L_s}{Q_L L_n L_s + j\omega_n(L_n + L_s)}\right| \frac{1}{|\mathbf{Z}_{\text{in}}(j\omega_n)|}. \tag{20}$$

The LLC steady-state analysis can be done using the normalized equations obtained in this section.

III. RESONANT FREQUENCIES OF THE $L3C2$ TOPOLOGY

It is crucial that the resonant circuit represents an inductive load, and that the current of the input-resonant circuit lags behind the output voltage of the half-bridge inverter. This means the input impedance phase, φ must be positive in all operating conditions. According to Fig. 1(b), ZVS conditions for the *LLC* resonant converter are guaranteed if the switching frequency is greater than the load resonant frequency. The lowest resonant frequency occurs for no-load conditions ($Q_L \rightarrow \infty$) and is defined as $f_{r,\text{oc1}}$. However, the *LLC* resonant converter cannot operate in high frequency due to the diodes parasitic capacitances in the secondary of the transformer. In the $L3C2$ resonant converter, there are two resonant frequencies for high Q_L, and as a result, two non-operating regions are imposed. According to Fig. 2(b), the first non-operating area is similar to that of the *LLC* resonant circuit. The second is after the short-circuit resonant frequency and just before the second open-circuit resonant frequency ($f_{r,\text{oc2}}$). In fact, in this region, the resonant circuit represents a capacitive load for high loaded quality factor, and the control circuit must be prevented from entering this region. Increasing the switching frequency above $f_{r,\text{oc2}}$ presents wide output voltage regulation for the $L3C2$ resonant converter, which is unobtainable for the *LLC*. In this section, the resonant frequencies of the $L3C2$ resonant circuit will be determined as a function of normalized parameters.

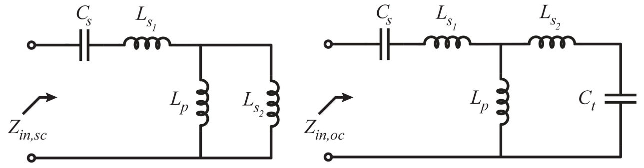

(a) (b)

Fig. 7. Equivalent circuit of the $L3C2$: (a) Output short-circuit condition, (b) Output open-circuit condition.

A. Short-Circuit Resonant Frequency

In short-circuit conditions, the value of output load tends to zero ($Q_L \rightarrow 0$) and the nonconduction angle is calculated as follows:

$$\psi = \lim_{Q_L \rightarrow 0} \cos^{-1} \frac{\pi - 2C_n Q_L \omega_n}{\pi + 2C_n Q_L \omega_n} = 0. \tag{21}$$

As a result, R_{eq} and C_{eq} are equal to zero, and the ac equivalent circuit of the $L3C2$ resonant converter is changed [see Fig. 7(a)]. Using the normalized parameters presented in (7), the input impedance of Fig. 7(a) is given by

$$Z_{\text{in,sc}}(j\omega_s) = \frac{1}{j\omega_s C_s} + j\omega_s L_{s_1} + (j\omega_s L_p)||j\omega_s L_{s_2} \tag{22}$$

$$\frac{Z_{\text{in,sc}}(j\omega_n)}{Z_0} = \frac{1-(1+\frac{1}{L_n+L_s})\omega_n^2}{j(\frac{1}{L_n}+\frac{1}{L_s})\omega_n} \tag{23}$$

and the short-circuit resonant frequency $f_{r,\text{sc}}$ is given by the following:

$$\frac{\omega_{r,\text{sc}}}{\omega_0} = \frac{1}{\sqrt{1+\frac{1}{L_n+L_s}}}. \tag{24}$$

B. Open-Circuit Resonant Frequency

In open-circuit conditions ($Q_L \rightarrow \infty$), the nonconduction angle and equivalent elements are obtained as follows:

$$\psi = \lim_{Q_L\rightarrow\infty} \cos^{-1}\frac{\pi - 2C_n Q_L \omega_n}{\pi + 2C_n Q_L \omega_n} = \pi \Rightarrow R_{\text{eq}}$$
$$= 0\,\&\,C_{\text{eq}} = C_t. \tag{25}$$

Fig. 7(b) shows the ac equivalent circuit of the $L3C2$ resonant converter in no-load conditions. Therefore, the input impedance of this circuit is given as follows:

$$Z_{\text{in,oc}}(j\omega_s) = \frac{1}{j\omega_s C_s} + j\omega_s L_{s_1} + (j\omega_s L_p)||\left(j\omega_s L_{s_2} + \frac{1}{j\omega_s C_t}\right) \tag{26}$$

As presented in Fig. 2(b), there are two open-circuit resonant frequencies in the $L3C2$ resonant circuit, and the final equations are presented as follows. The obtained equations for open-circuit resonant frequencies are very useful to determine the operating region of the $L3C2$ resonant converter.

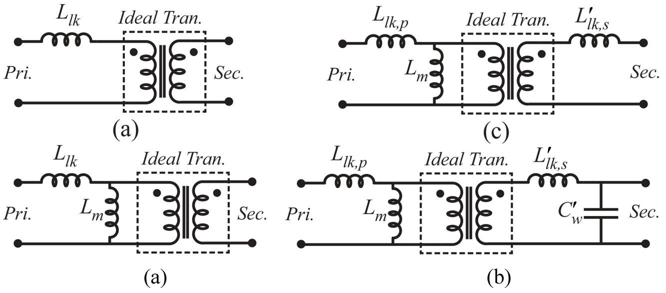

Fig. 8. Transformer models, (a) first order, (b) second order, (c) third order, and (d) fourth order.

IV. SECONDARY LEAKAGE INDUCTANCE EFFECT ON $L3C2$ RESONANT CONVERTER

In order to analyze the converters, transformers are typically modeled by an equivalent circuit based on the operating frequency of the converter and transformer configuration. Fig. 8 presents different standard equivalent circuits of the transformer that have been used in the literature for converters analysis. Interleaving the windings leads to high coupling between primary and secondary and as a result the lowest amount of leakage inductance obtains, which means the first- or second-order model of the transformer can be used [see Fig. 8(a) and (b)] [6], [36]. On the other hand, applying a sectional bobbin with an air gap between core halves leads to less coupling between windings and increases leakage inductance in both primary and secondary sides of the transformer, which is desirable in resonant converters to integrate the series-resonant inductance into the transformer [see Fig. 8(c)]. This model is widely used for analysis of resonant converters [23], [37], [38]. In this paper, due to the wide operating frequency, the fourth-order equivalent circuit of the transformer, as shown in Fig. 8(d), is adopted to accurately analyze the converter. This equivalent circuit takes into account the effects of the primary and the secondary leakage inductance separately. Also, the magnetizing inductance and the secondary winding capacitance are incorporated in this equivalent circuit.

$$\frac{Z_{\text{in,oc}}(j\omega_n)}{Z_0} = \frac{\left(\frac{C_n}{L_n}+\frac{C_n}{L_s}+\frac{C_n}{L_n L_s}\right)\omega_n^4 - \left(\frac{C_n}{L_n}+\frac{C_n}{L_s}+\frac{1}{L_n}+1\right)\omega_n^2 + 1}{j\left(1-(\frac{1}{L_n}+\frac{1}{L_s})\omega_n^2\right)\omega_n}. \tag{27}$$

$$\frac{\omega_{r,\text{oc1}}}{\omega_0} = \sqrt{\frac{\frac{C_n}{L_n}+\frac{C_n}{L_s}+\frac{1}{L_n}+1-\sqrt{\left(\frac{C_n}{L_n}+\frac{C_n}{L_s}+\frac{1}{L_n}+1\right)^2 - 4\left(\frac{C_n}{L_n}+\frac{C_n}{L_s}+\frac{C_n}{L_n L_s}\right)}}{2\left(\frac{C_n}{L_n}+\frac{C_n}{L_s}+\frac{C_n}{L_n L_s}\right)}} \tag{28}$$

$$\frac{\omega_{r,\text{oc2}}}{\omega_0} = \sqrt{\frac{\frac{C_n}{L_n}+\frac{C_n}{L_s}+\frac{1}{L_n}+1+\sqrt{\left(\frac{C_n}{L_n}+\frac{C_n}{L_s}+\frac{1}{L_n}+1\right)^2 - 4\left(\frac{C_n}{L_n}+\frac{C_n}{L_s}+\frac{C_n}{L_n L_s}\right)}}{2\left(\frac{C_n}{L_n}+\frac{C_n}{L_s}+\frac{C_n}{L_n L_s}\right)}}. \tag{29}$$

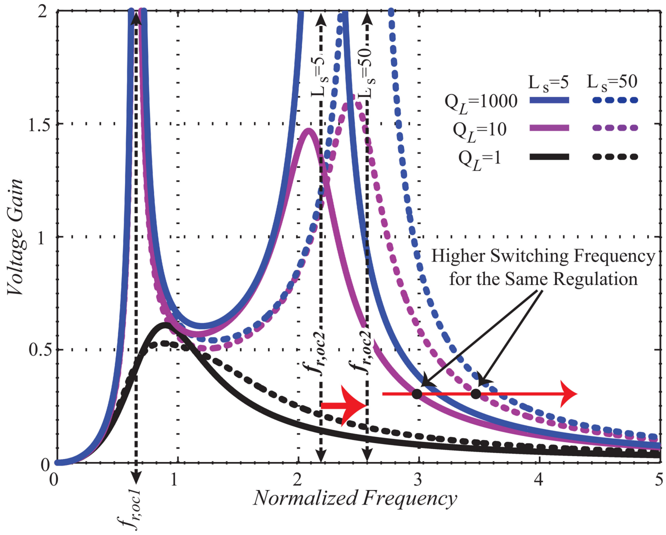

Fig. 9. Effect of secondary leakage inductance on the voltage gain curves.

Beside the more accurate steady-state analysis, which is derived in this paper, the transformer secondary leakage inductance plays an important role in the required switching frequency range of the $L3C2$ resonant converter. Fig. 9 shows the effect of secondary leakage inductance on the voltage gains of the $L3C2$ resonant converter. According to this figure, high amount of secondary leakage inductance (low value of L_s) leads to moving the second resonant frequency closer to the first one, and therefore, wide output voltage regulation is obtainable. In other words, for the proposed resonant converter with low secondary leakage inductance, switching frequency needs to increase more in comparison with high secondary leakage inductance for getting the same output voltage regulation.

V. DESIGN OF EXPERIMENT (DOE) METHODOLOGY

The optimized selection of normalized parameters should be performed according to the application requirements. In this paper, due to the battery charger application, the main object during design procedure is to design *LLC* and $L3C2$ in such a way as to obtain maximum output voltage regulation, while providing soft switching conditions, and minimizing circulating current. According to the steady-state analysis performed in Section II. the equations obtained for *LLC* and $L3C2$ resonant converter are functions of three and four normalized variables, respectively. Therefore, the desired normalized parameters should be interchangeable, making the design a multidimensional optimization problem with multiple tradeoff challenges. In this section, statistical DoE methodology is employed to consider the behavior of both resonant converters when responding to variations in different normalized parameters. This methodology provides a systematic approach for applying statistics to experimentation in order to achieve efficient and accurate results [39], [40]. The output response surfaces of DoE have been selected based on the most important attributes for a battery charger application, which are high efficiency and a wide output voltage converter. In the following sections, these attributes will be discussed in detail.

A. Minimum Obtainable Output Voltage

To respond to charge algorithm in different states of charge, the charger should regulate the output voltage from near zero up to 1.5 times the nominal voltage. As a result, maximum output voltage regulation is the most important attribute that should be considered. According to Figs. 1 and 2, the voltage gain curves are not the same in the *LLC* and $L3C2$ resonant converters, and because of this, two different criteria are introduced for output voltage regulation. The output response surfaces are based on the optimization of the following criteria:

$$\begin{cases} \left| \left. \dfrac{\partial M_v}{\partial f_n} \right|_{f_n = f_{r,\mathrm{sc}}} \right| \rightarrow \text{Maximize}, & \text{for} \quad LLC \\ \dfrac{V_{\mathrm{out},m,NL}}{V_{\mathrm{out},n}} \rightarrow \text{Minimize}, & \text{for} \quad L3C2. \end{cases} \tag{30}$$

According to (30) and Fig. 1, the *LLC* voltage gain curves can approach nearly zero voltage in high frequency when the absolute value of the gain curves' slope at the short-circuit resonant frequency is set to be maximized. For the $L3C2$ resonant converter, the ratio between minimum output voltage gain in no-load condition (maximum switching frequency) and nominal output voltage is calculated.

B. Resonant Circuit Current

In order to attain high efficiency in part load condition, the difference between input-resonant circuit current in nominal and no-load condition should be maximized [26]. In other words, the less circulating current, the greater part load efficiency. Equation (31) presents the second output of DoE that should be maximized

$$\frac{I_{L_{s1},FL}}{I_{L_{s1},NL}} \rightarrow \text{Maximize}. \tag{31}$$

C. Soft Switching Operating Condition

In order to provide soft switching conditions for power MOSFETs, the phase angle of input impedance should be positive. On the other hand, if this angle is too steep in the nominal load condition, the current stress on semiconductor devices and other passive elements will be increased. Equation (32) presents the range of input impedance phases that the output response of DoE should fall within

$$\begin{cases} \varphi > 15^\circ, & \text{for practical margin} \\ \varphi < 30^\circ, & \text{for high-efficiency achievement.} \end{cases} \tag{32}$$

In the following paragraphs, the output response surfaces of DoE will be considered. Table I presents the range for normalized parameters, which will be used as the input range of normalized parameters in DoE. The performances of carefully selected data points within these ranges of factors have been investigated for the $L3C2$ and *LLC* resonant converters. The $L3C2$ requires 25 simulations to cover the effects of four normalized parameters, while the *LLC* converter used 15 points to

TABLE I
NORMALIZED PARAMETER RANGE AND SELECTED VALUE

Par.	*LLC*		*L3C2*	
	Range	Selected	Range	Selected
L_n	[0.2–0.8]	0.4	[0.25–1.25]	0.9
L_s	[3–10]	4.4	[3–10]	4.7
C_n	$***$	$***$	[0.1–0.5]	0.3
Q_L	[0.5–1.5]	1	[0.5–1.5]	1

study the impact of three normalized parameters. Significance testing was combined with ANOVA regression to develop 3-D response surfaces for each of the three main attributes listed above [39]. The response surfaces for *LLC* and $L3C2$ resonant converters have been presented in Figs. 10 and 11, respectively. It is necessary to mention that each surface response has been drawn based on the two normalized parameters that have the most impact on the surface.

Now, it is possible to select normalized parameters for each resonant converter by considering the different response surfaces at the same time. According to Fig. 10(a), in order to satisfy (30), the L_n and L_s should be, respectively, at the highest and lowest possible levels. Two ranges can be defined for normalized parameters (gray band), and the points located in the common area (dark gray) are candidates for optimum L_n and L_s parameters. The same concept can be applied to other surfaces of Fig. 10 with respect to (31) and (32), and finally, the intersection between different common areas determines the values of normalized parameters. The same routine has been employed in order to select the normalized value of the $L3C2$ resonant converter. The final values of normalized parameters have been selected after conducting simulations and taking into account practical considerations, especially the amount of secondary leakage inductance. According to Figs. 10(a) and 11(a), secondary leakage inductance on both resonant converters under consideration has a positive effect on output voltage regulation. This means that a high amount of secondary leakage inductance (low value of L_s) can expand the output voltage regulation.

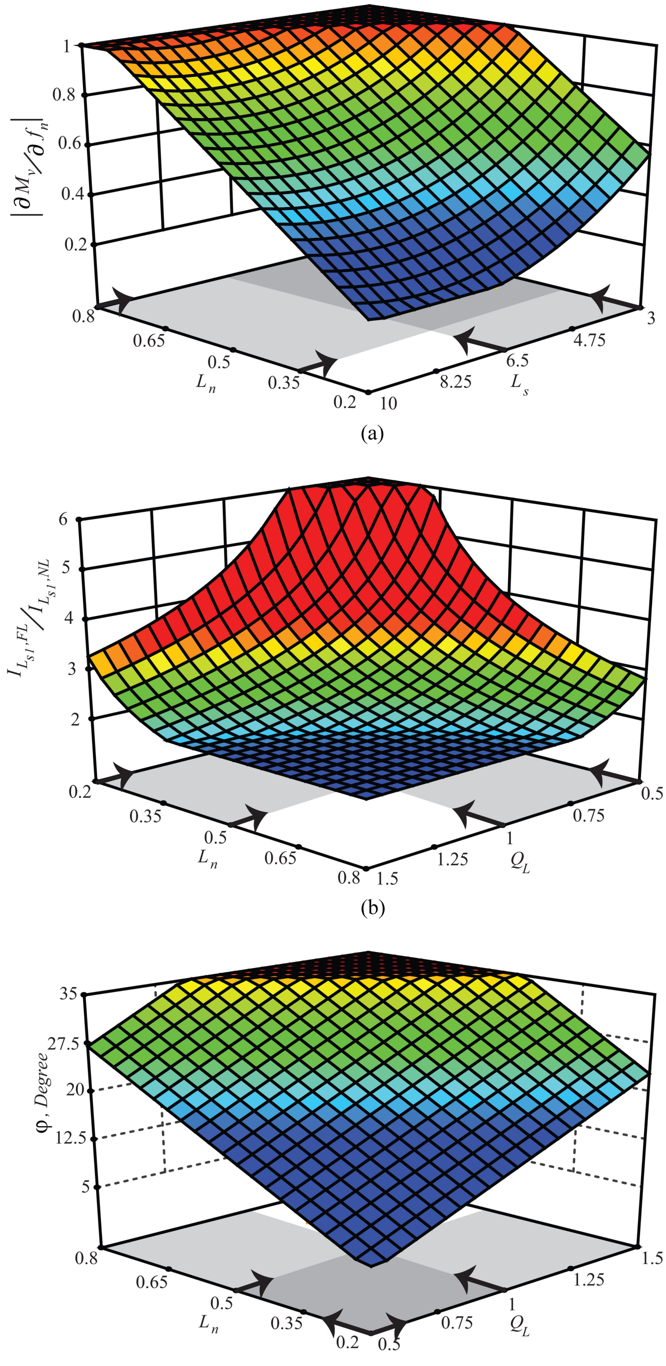

(a)

(b)

(c)

Fig. 10. DoE response surfaces for *LLC* resonant converter: (a) Voltage gain slope surface versus L_n and L_s, (b) input-resonant circuit current ratio versus L_n and Q_L, and (c) phase of the input impedance versus L_n and Q_L.

VI. RESONANT CONVERTER DESIGN

In this section, based on optimized selection of normalized parameters, the voltage gain curves of the resonant converter will be used to design two power converters with the same input–output specifications and switching frequency variations.

A. $L3C2$

Fig. 12 presents the voltage transfer function M_v, first series inductance current $I_{L_{s_1}}$, and the input impedance phase φ versus frequency for $L_n = 0.9$, $L_s = 4.7$, and $C_n = 0.3$. As observed in Fig. 12(a), the minimum switching frequency is determined by the maximum output voltage in nominal output power ($Q_L = 2.2$) located between $f_{r,\mathrm{oc1}}$ and $f_{r,\mathrm{sc}}$. In order to obtain high efficiency in nominal load conditions, the circulating current must be minimal. According to Fig. 12(b), the amplitude of the switchs' current decreases drastically in higher Q_L when the switching frequency is around f_0. Moreover, the voltage gain is independent from the load (no-load conditions are exceptional) means minimum switching variation in nominal output voltage. This point is selected for nominal load operation ($Q_L = 1$). The minimum required output voltage in no-load conditions defines the maximum switching frequency ($Q_L = 1000$). According to Fig 12(a), it is possible to increase the switching frequency in order to decrease the output voltage to zero. Fig. 12(c) presents

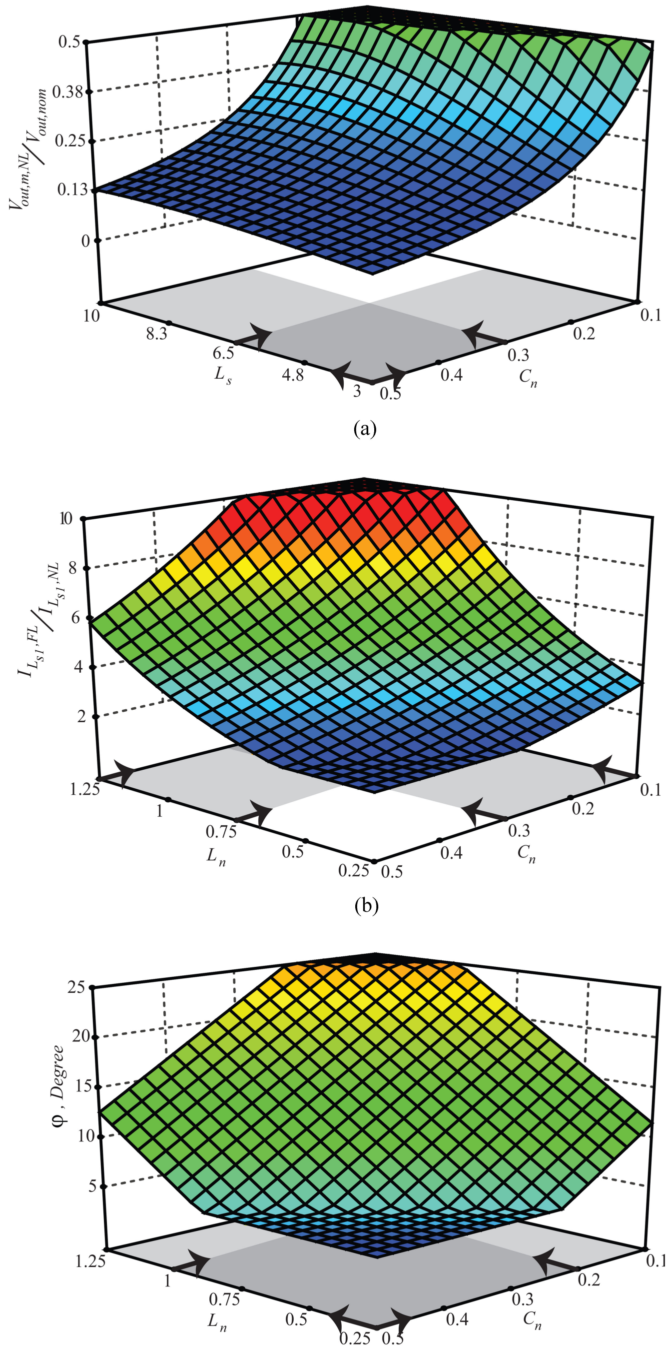

(a)

(b)

(c)

Fig. 11. DoE response surfaces for $L3C2$ resonant converter: (a) Voltage gain ratio surface versus L_s and C_n, (b) input-resonant circuit current ratio versus L_n and C_n, and (c) phase of the input impedance versus L_n and C_n.

the phase of the resonant circuit input impedance, φ versus frequency for different load conditions. In order to obtain high efficiency and provide a noise-free output voltage, soft switching is necessary for the power MOSFETs. Therefore, it is vital that the resonant circuit behaves like an inductive load. According to Fig. 12(c), between the minimum and maximum switching frequency there is a nonoperating area for high Q_L. Except for in the mentioned nonoperating area, the resonant circuit works in inductive regions and ZVS is provided for the half-

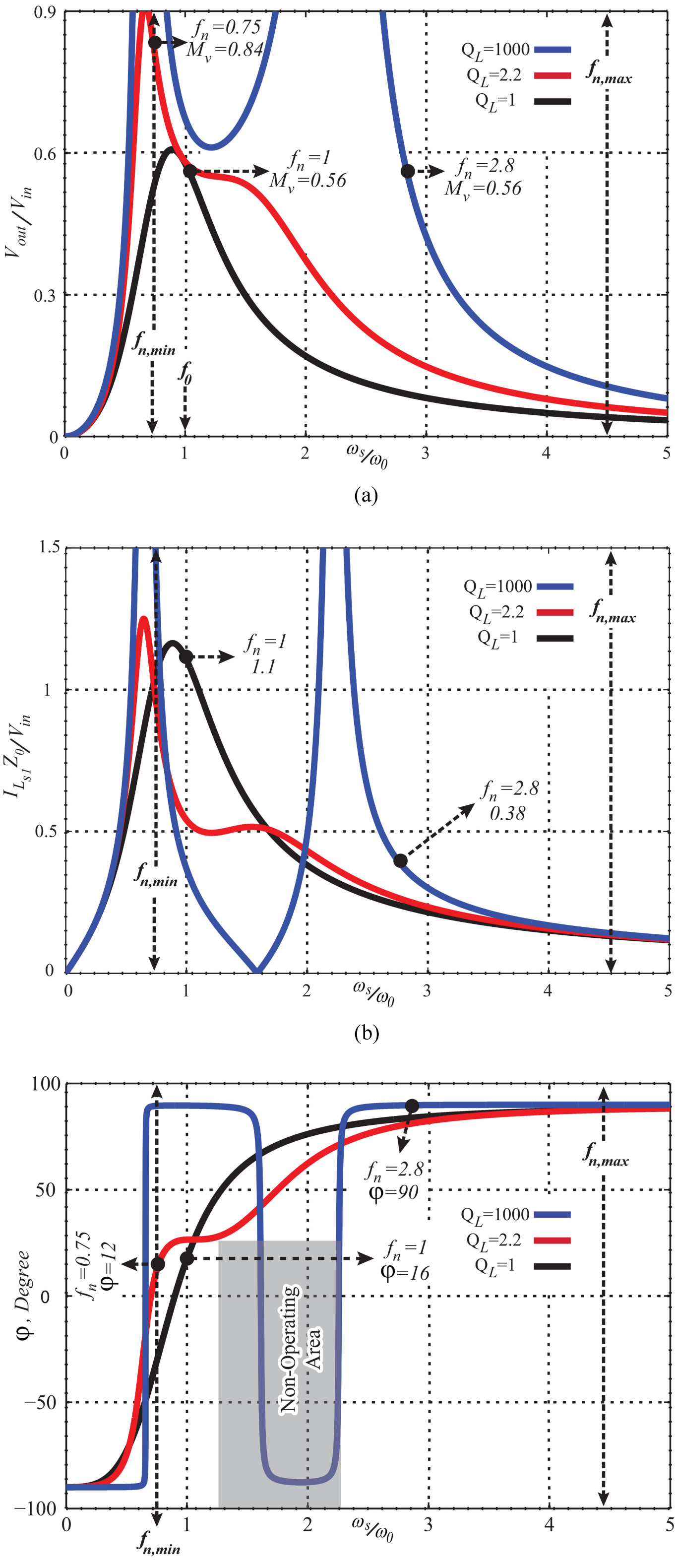

(a)

(b)

(c)

Fig. 12. FHA analysis of the $L3C2$ resonant converter with capacitive output filter for $L_s = 4.7$, $L_n = 0.9$ and $C_n = 0.3$, and constant values of normalized load resistances (Q_L): (a) Magnitude of voltage transfer function (M_v), (b) amplitude of the normalized first series inductance current ($I_{L_{S_1}}$), and (c) phase of the input impedance (φ).

bridge inverter. In the following, the $L3C2$ resonant circuit elements are calculated based on the voltage transfer function curves and the power charger specifications including the input voltage, output voltage, output power, and switching frequency variations. The main specifications of the battery charger are considered as follows:

$$V_{\text{in}} = 400\,\text{VDC},\ V'_{\text{out}} = 96\,\text{VDC}$$
$$P_{\text{out}} = 950\,\text{W},\ f_s = 100 - 600\,\text{kHz}. \quad (33)$$

According to Fig. 12(a), the minimum normalized switching frequency is equal to 0.75. As a result, the series-resonant frequency is given by the following equation:

$$f_{n,\min} = 0.75,\ f_{s,\min} = 100\,\text{kHz},\ f_n = \frac{f_s}{f_0} \Rightarrow f_0 = 133\,\text{kHz}. \quad (34)$$

The voltage gain at $f_n = 1$ and the nominal load conditions are given as follows:

$$M_v = 0.56 \text{ for } Q_L = 1,\ L_n = 0.9,\ L_s = 4.7,\ C_n = 0.3. \quad (35)$$

Therefore, the parallel capacitor voltage (output voltage) and transformer turns ratio are calculated as follows:

$$V_{\text{out},n} = M_v.V_{\text{in}} = 0.56 * 400 = 224\,\text{VDC}$$
$$n = \frac{N_p}{N_s} = \frac{V_{\text{out},n}}{V'_{\text{out},n}} \Rightarrow n = \frac{224}{96} = 2.33. \quad (36)$$

According to (7) and (33), the characteristic impedance is given by

$$R_L = \frac{{V_{\text{out}}}^2}{P_{\text{out}}},\ Z_0 = \frac{R_L}{Q_L} \Rightarrow Z_0 = \frac{{V_{\text{out}}}^2}{P_{\text{out}} Q_L} = 53\,\Omega. \quad (37)$$

Therefore, the resonant components are obtained as follows:

$$\omega_0 = \frac{\omega_s}{\omega_n} = 266\,\pi e^3 \Rightarrow L_{s_1} = \frac{Z_0}{\omega_0} = 63\,\mu\text{H}$$
$$C_s = \frac{1}{Z_0.\omega_0} = 23\,\text{nF},\ L_{s_2} = \frac{L_{s_1}}{L_s} = 13\,\mu\text{H}$$
$$L_p = \frac{L_{s_1}}{L_n} = 70\,\mu\text{H},\ C_p = C_n.C_s = 6.9\,\text{nF}. \quad (38)$$

The $L3C2$ resonant circuit parameters used in the simulation results and experimental prototype are summarized in Table II.

B. LLC

Fig. 13 shows the voltage transfer function M_v, first series inductance current $I_{L_{s_1}}$, and the input impedance phase φ versus frequency for $L_n = 0.4$, and $L_s = 4.4$. As indicated in Fig 13(a), the minimum normalized switching frequency is equal to 0.69. Therefore, the series-resonant frequency is calculated using the following equation:

$$f_{n,\min} = 0.69,\ f_{s,\min} = 100\,\text{kHz},\ f_n = \frac{f_s}{f_0} \Rightarrow f_0 = 145\,\text{kHz}. \quad (39)$$

In nominal load conditions ($Q_L = 1$) the voltage gain is equal to 0.52 and, as a result, transformer turns ratio is obtained as

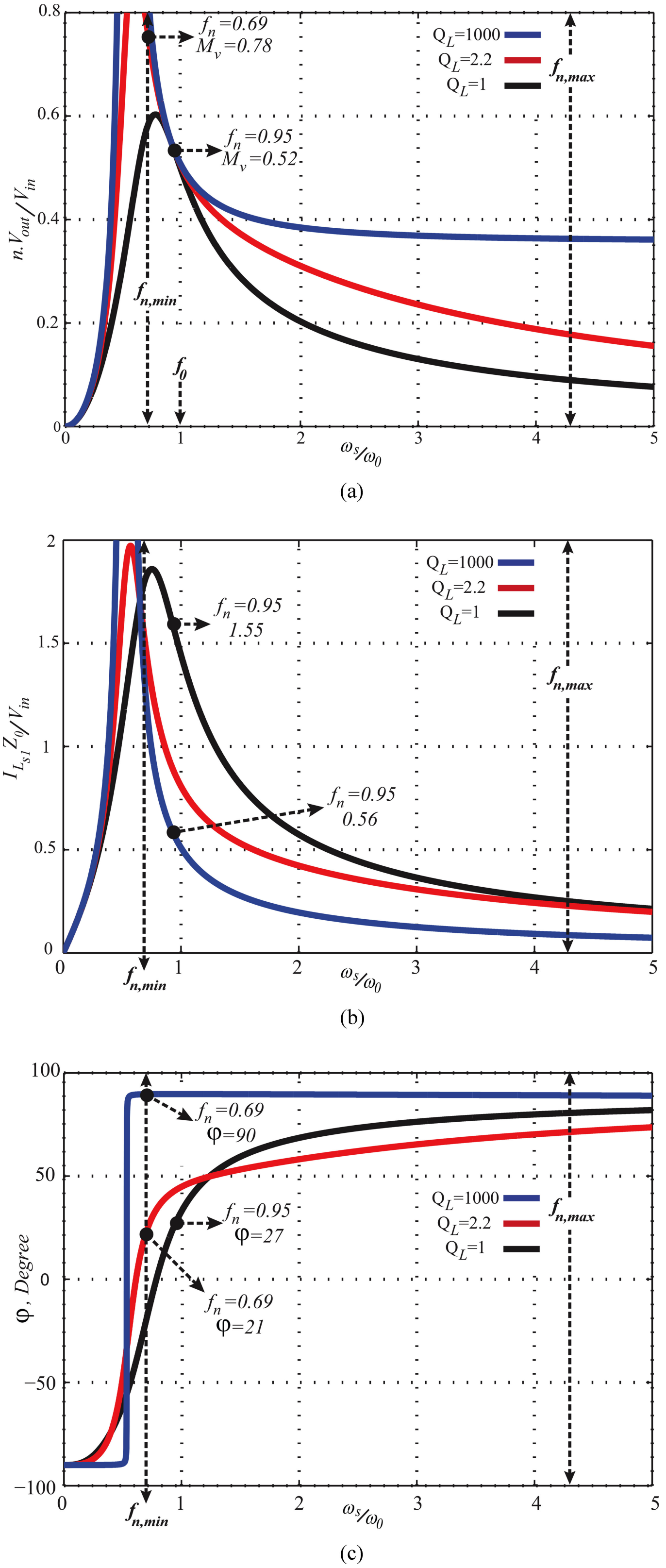

Fig. 13. FHA analysis of the *LLC* resonant converter for $L_s = 4.4$, and $L_n = 0.4$, with constant values for normalized load resistances (Q_L): (a) Magnitude of voltage transfer function (M_v), (b) amplitude of the normalized first series inductance current ($I_{L_{S_1}}$), and (c) phase of the input impedance (φ).

TABLE II
LLC AND $L3C2$ RESONANT CONVERTERS PARAMETERS

Parameters	*LLC*	$L3C2$
V_{in}	$400\,\mathrm{VDC}$	$400\,\mathrm{VDC}$
$V'_{\mathrm{out},n}$	$96\,\mathrm{VDC}$	$96\,\mathrm{VDC}$
$V'_{\mathrm{out,max}}$	$144\,\mathrm{VDC}$	$144\,\mathrm{VDC}$
P_{out}	$950\,\mathrm{W}$	$950\,\mathrm{W}$
f_s Range	$100-600\,\mathrm{kHz}$	$100-600\,\mathrm{kHz}$
f_0	$145\mathrm{kHz}$	$133\mathrm{kHz}$
C_s	$30\,\mathrm{nF}$	$23\,\mathrm{nF}$
C'_p	$***$	$40\,\mathrm{nF}$
L_{s_1}	$41\,\mu\mathrm{H}$	$63\,\mu\mathrm{H}$
L_{s_2}	$9\,\mu\mathrm{H}$	$13\,\mu\mathrm{H}$
L_p	$103\,\mu\mathrm{H}$	$70\,\mu\mathrm{H}$
$n = \frac{N_p}{N_s}$	2.17	2.33

follows:

$$n = \frac{N_p}{N_s} = \frac{V_{\mathrm{out},n}}{V'_{\mathrm{out},n}} = \frac{M_v.V_{\mathrm{in}}}{V'_{\mathrm{out}}} = 2.17. \tag{40}$$

In the *LLC* resonant converter with capacitive output filter, the equivalent resistance is obtained using (16) and is equal to

$$R'_L = \frac{{V'_{\mathrm{out}}}^2}{Pout} = 9.7\,\Omega \Rightarrow R'_{\mathrm{eq}} = 7.9\,\Omega,\; R_{\mathrm{eq}} = n^2 R'_{\mathrm{eq}} = 37.2\,\Omega. \tag{41}$$

The resonant circuit elements of the *LLC* resonant circuit are calculated as follows:

$$Z_0 = \frac{R_{\mathrm{eq}}}{Q_L} = 37.2\,\Omega,\; \omega_0 = \frac{\omega_s}{\omega_n} = 290\,\pi e^3 \tag{42}$$

$$\Rightarrow L_{s_1} = \frac{Z_0}{\omega_0} = 41\,\mu\mathrm{H},\; C_s = \frac{1}{Z_0.\omega_0} = 30\,\mathrm{nF} \tag{43}$$

$$L_{s_2} = 9\,\mu\mathrm{H},\; L_p = 103\,\mu\mathrm{H}. \tag{44}$$

The circuit parameters for the *LLC* resonant converter are provided in Table II. According to Fig. 13(c), the input-resonant phase of the *LLC* is positive for the mentioned range of the switching frequency, and the resonant circuit represents an inductive load. As a result, ZVS is guaranteed for all loads and output voltage conditions. Comparing the converters elements collected in Table II reveals that the only extra element in the proposed $L3C2$ resonant converter is the parallel resonant capacitor put in the transformer secondary side.

VII. SIMULATION AND EXPERIMENTAL RESULTS

In order to investigate and compare the performance of the designed resonant converters, software simulation and prototype platforms have been employed to extract the voltage gains under different load conditions. The components, which are used in the prototypes, are shown in Tables III. Also, the test setup picture is presented in Fig. 14. The selected switching frequency is between 100 and 600 kHz, and the frequency span for the voltage gain curves is 10 kHz, which means more than 50 points have been extracted in each drawing. The simulation and experimental results are presented in Fig. 15. There are several limitations indicated in each figure, including minimum and maximum switching frequencies, the maximum output power, and the maximum output voltage. The simulation and experimental results are presented in solid and dotted shapes, respectively. As predicted by the theory, the $L3C2$ provides an extended frequency operating range. Fig. 15 presents the results for the *LLC* and $L3C2$ resonant converters under three different load conditions. According to Fig. 15(a), in the *LLC* resonant converter, the simulation and experimental results are almost the same for $R'_L = 9.75\,\Omega$ and $R'_L = 21.9\Omega$. But for no-load condition in the *LLC* resonant converter, there is a discrepancy between simulation and experimental results. In fact, for switching frequency higher than 300kHz, the effect of the output diodes junction capacitances leads to increased output voltage in the *LLC*. As observed in Fig. 15(b), in the $L3C2$ resonant converter, the simulation and experimental voltage gains have good fit for different load conditions. The analytical equations obtained based on FHA can precisely predict the behavior of the multiresonant $L3C2$ resonant converter with capacitive output filter for a wide range of output voltages and loads [as already depicted in Fig. 12(a)].

TABLE III
COMPONENTS OF RESONANT CONVERTER PLATFORMS

Component	Part Number	Ratings
Inverter MOSFET's	$IXFX64N60$	$600\mathrm{VDC}, 64\mathrm{A}$
Series-Resonant Cap.	Film Cap.	$10\mathrm{nF}, 2000\mathrm{VDC}$
Series-Resonant Ind.	$3F3$	$***$
Transformer	$3F3$	$***$
Parallel Resonant Cap.	Film Cap.	$10\mathrm{nF}, 1000\mathrm{VDC}$
Rectifier Diode	MBR40250	$250\mathrm{VDC}, 40\mathrm{A}$
Output Cap.	Film Cap.	$1.5\mathrm{uF}, 250\mathrm{VDC}$

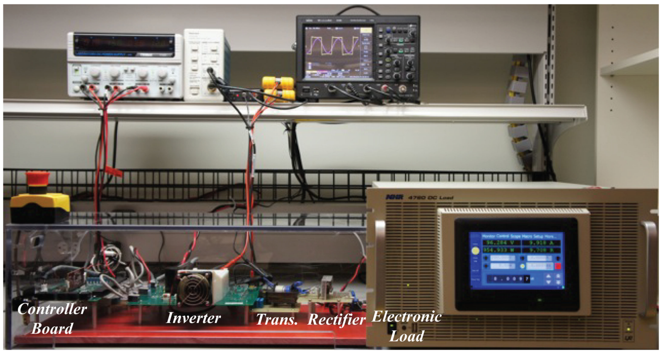

Fig. 14. Prototype test platform of the resonant power converters.

In order to provide high-quality output voltage and maximize the converter efficiency, it is vital to realize soft commutation for the output rectifier diodes. Basically, the reverse recovery current of output rectifier diodes during the turn-off transition leads to high voltage peak across output diodes and as a result, diodes with more withstand voltage should be selected, which means more conduction losses. The *LLC* and $L3C2$ converters can provide ZCS for output diodes for wide variation of switching frequency. Fig. 16(a) and (b) shows the experimental waveforms of the voltage and current on the secondary side of the transformer in the *LLC* resonant converters for two full power

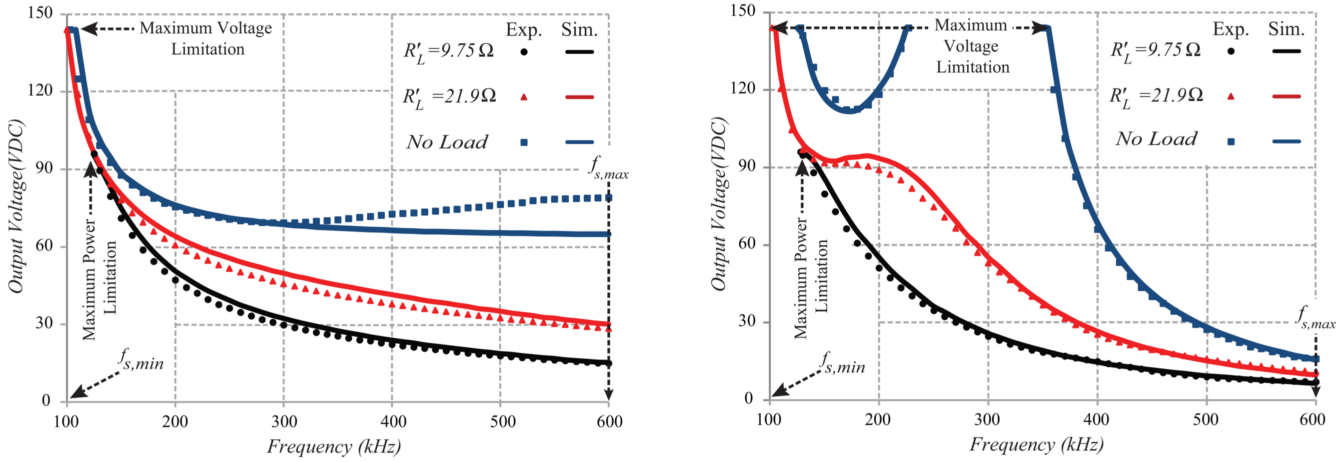

(a)

(b)

Fig. 15. Simulation and experimental results for dc voltage gain versus frequency. (a) *LLC* resonant converter, and (b) *L3C2* resonant converter.

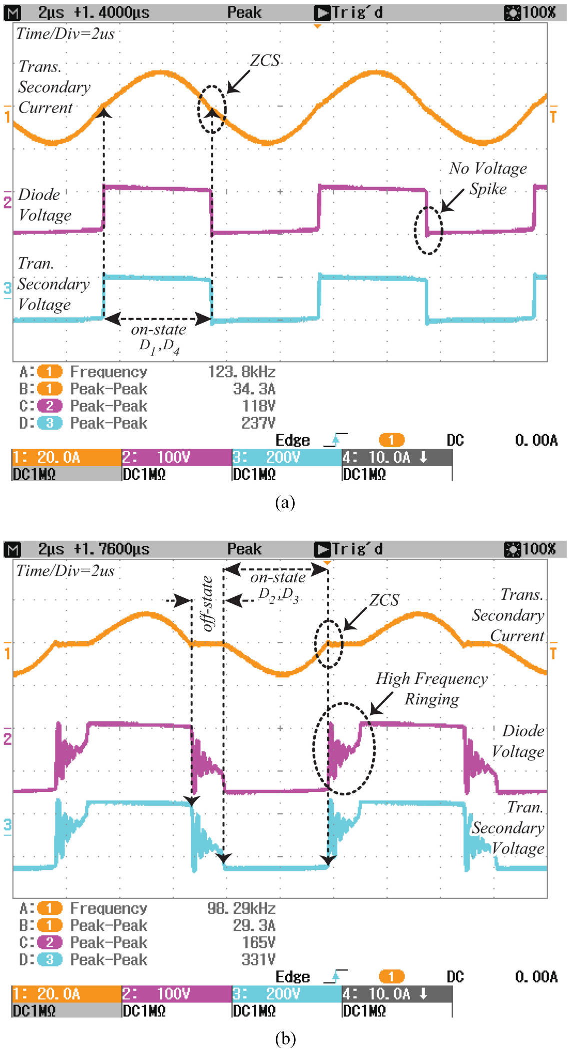

(a)

(b)

Fig. 16. *LLC* transformer secondary-side waveforms: (a) $V_{\text{out}} = 96$ VDC and $P_{\text{out}} = 950$ W, and (b) $V_{\text{out}} = 144$ VDC and $P_{\text{out}} = 950$ W (High voltage, high-frequency ringing for this condition).

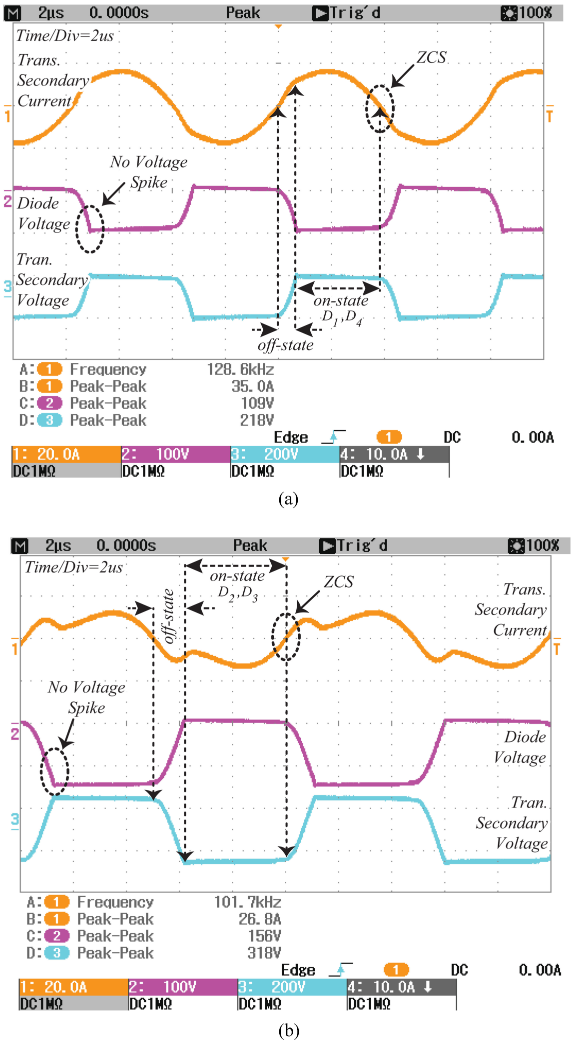

(a)

(b)

Fig. 17. *L3C2* transformer secondary-side waveforms: (a) $V_{\text{out}} = 96$ VDC and $P_{\text{out}} = 950$ W, and (b) $V_{\text{out}} = 144$ VDC and $P_{\text{out}} = 950$ W (Elimination of the high-frequency ringing).

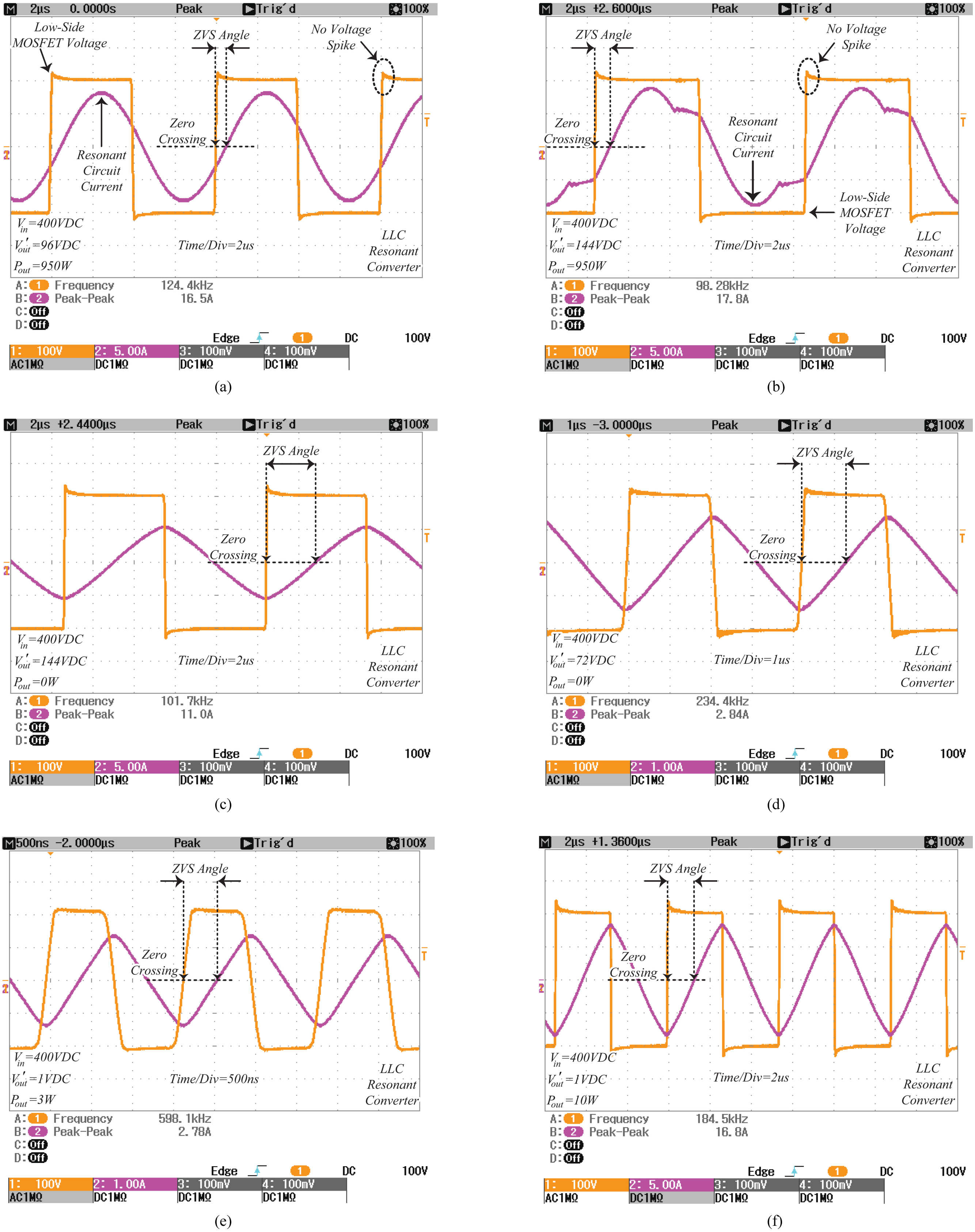

Fig. 18. Experimental results for the *LLC* resonant converter, drain–source voltage for low-side MOSFET in half-bridge inverter (S_2) and first series-resonant inductor current ($I_{L_{s_1}}$): (a) $V_{\text{out}} = 96$ VDC and $P_{\text{out}} = 950$ W, (b) $V_{\text{out}} = 144$ VDC and $P_{\text{out}} = 950$ W, (c) $V_{\text{out}} = 144$ VDC and $P_{\text{out}} = 0$ W, (d) $V_{\text{out}} = 72$ VDC and $P_{\text{out}} = 0$ W, (e) $V_{\text{out}} = 1$ VDC and $P_{\text{out}} = 3$ W, and (f) $V_{\text{out}} = 1$ VDC and $P_{\text{out}} = 10$ W.

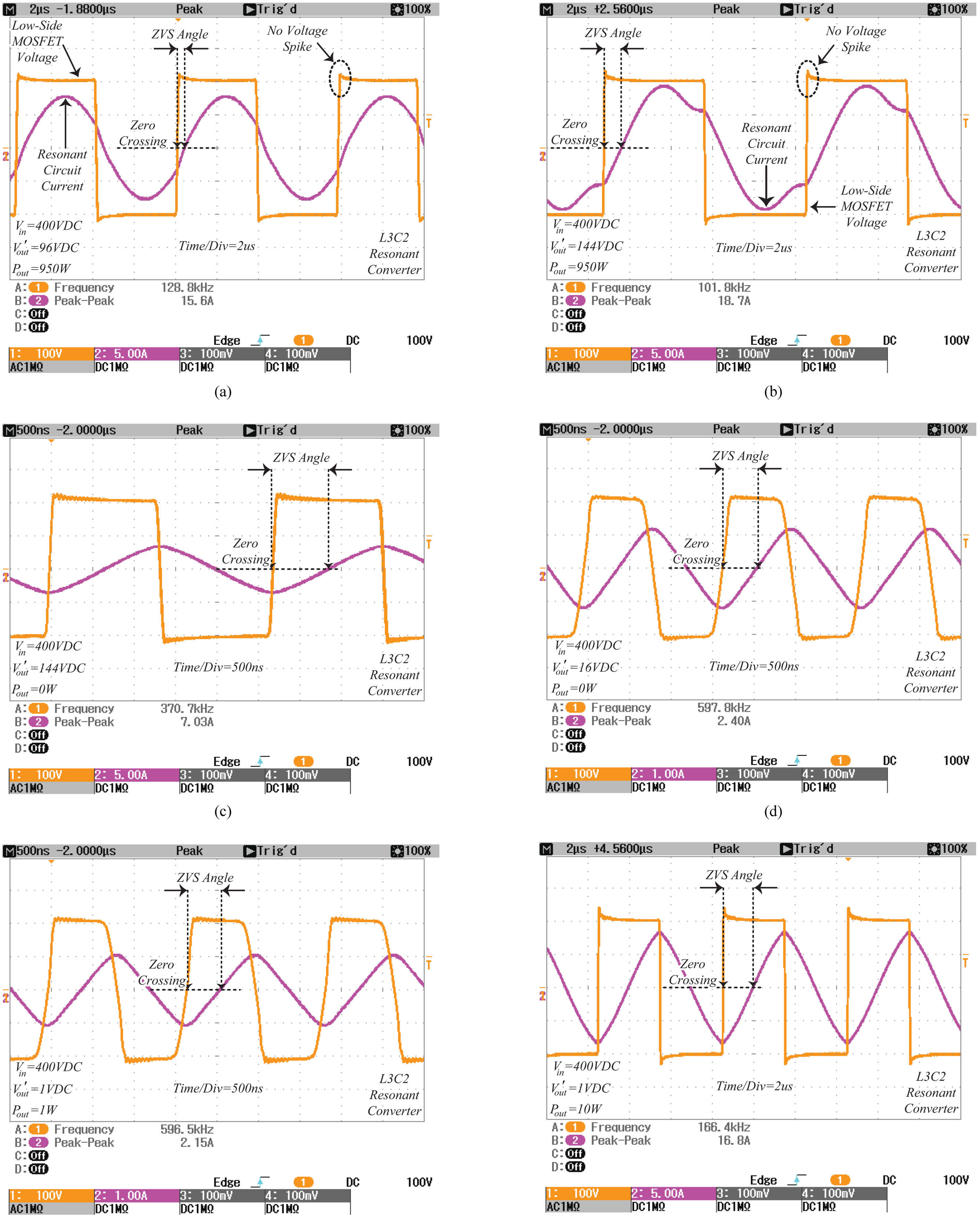

(a) (b) (c) (d) (e) (f)

Fig. 19. Experimental results for the $L3C2$ resonant converter, drain–source voltage for low-side MOSFET in half-bridge inverter (S_2) and first series-resonant inductor current ($I_{L_{s_1}}$): (a) $V_{\rm out} = 96$ VDC and $P_{\rm out} = 950$ W, (b) $V_{\rm out} = 144$ VDC and $P_{\rm out} = 950$ W, (c) $V_{\rm out} = 144$ VDC and $P_{\rm out} = 0\ W$, (d) $V_{\rm out} = 16$ VDC and $P_{\rm out} = 0$ W, (e) $V_{\rm out} = 1$ VDC and $P_{\rm out} = 1$ W, and (f) $V_{\rm out} = 1$ VDC and $P_{\rm out} = 10$ W.

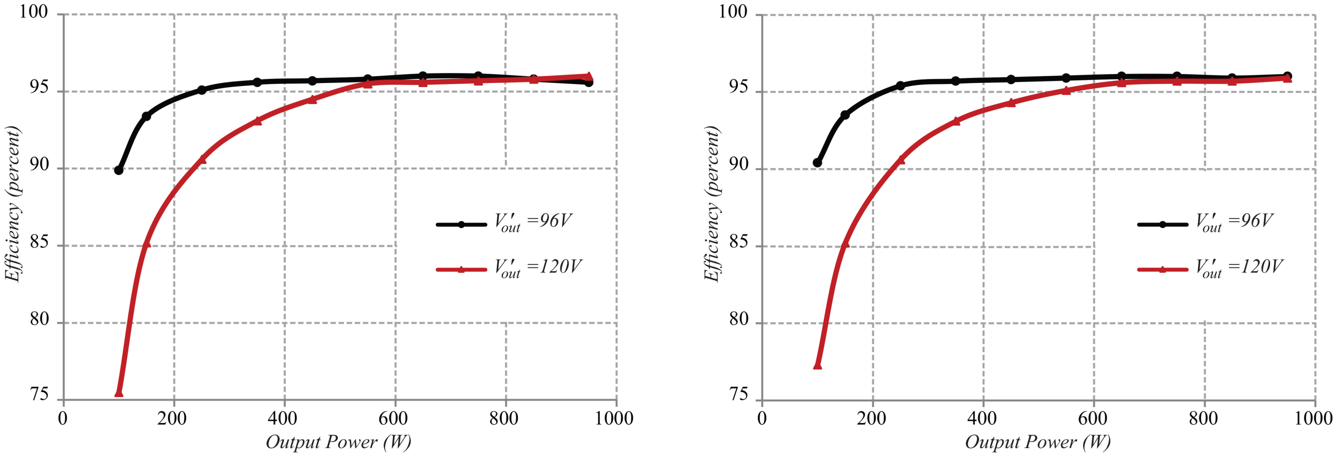

(a) (b)

Fig. 20. Efficiency curves at fixed output voltages: (a) *LLC* resonant converter, and (b) $L3C2$ resonant converter.

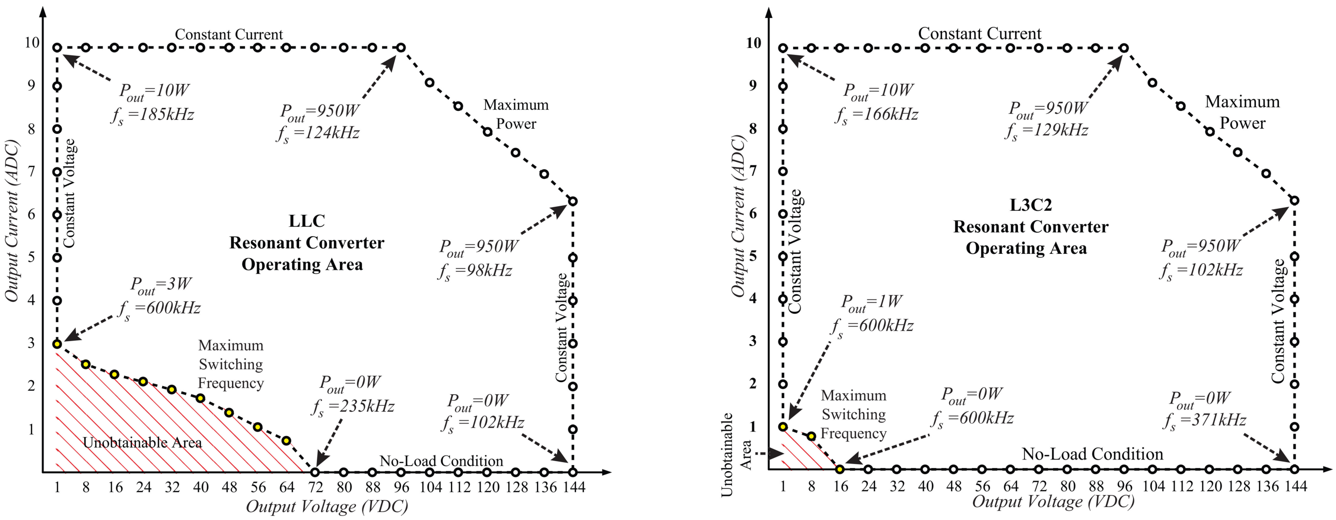

(a) (b)

Fig. 21. Obtained *V–I* plane from two considered resonant converters: (a) *LLC* resonant converter, and (b) $L3C2$ resonant converter.

conditions. According to these figures, ZCS is provided for output rectifier diodes, and voltage peak is eliminated. However, in the *LLC* resonant converter for switching frequency below and far from $f_{r,\text{sc}}$ (around the minimum switching frequency) and during the off-state intervals of the output rectifier diodes, high-voltage, high-frequency ringings exist across the rectifier diodes, which decrease the quality of the output voltage and increase the EMI. The proposed $L3C2$ design overcomes this issue and results in reduced ringing. According to the operating modes of the $L3C2$ output rectifier, as indicated in Fig. 4, in the end of power transfer interval, once $i_{L_{s_2}}$ reaches zero, the output diodes current smoothly reaches zero. This causes ZCS at turn-off and avoids any reverse recovery losses in the output diodes. In addition, the voltage across the diodes is smooth and sinusoidal during the switching transitions which leads to minimum negative impact of the diode junction capacitance in transient time. Fig. 17(a) and (b) presents the transformer secondary-side waveforms extracted from the $L3C2$ resonant converter platform. The experimental results for two full-load conditions prove the soft switching transient in turn-on and turn-off conditions without any high-frequency ringing.

Figs. 18 and 19 present the voltage and current waveforms extracted from experimental platforms of the *LLC* and $L3C2$ resonant converters, respectively. In each figure, drain–source voltage of the low-side MOSFET and the first series inductor current (MOSFETs current) are illustrated for different conditions. According to these figures, the zero crossings of the resonant circuit input current is within the low-side MOSFET voltage pulse and, as a result, in all of the presented conditions, the half-bridge switches are fully turned ON under zero voltage. Therefore, both the *LLC* and the $L3C2$ achieve soft switching transitions.

VIII. COMPARISON OF THE *LLC* AND $L3C2$ AS A BATTERY CHARGER

In this section, two main aspects of the studied resonant converters are considered, including the efficiency curves and obtainable *V–I* planes. One of the main advantages of resonant converters is soft switching, which leads to high-switching frequency and high-power density. In addition, ZVS is necessary to provide a low-noise environment which improves the quality of the output voltage. Fig. 20 presents the efficiency curves of the *LLC* and $L3C2$ resonant converters for two different output voltages. According to these curves, the designed resonant converters present an efficiency higher than 95% for an output power greater than $500\mathrm{W}$, and the maximum efficiency for both cases is 96%.

In the following, the *V–I* planes of the *LLC* and $L3C2$ are obtained in order to investigate the maximum coverage region. As mentioned in Section I, the battery charger must be able to respond to different modes of the charge algorithms and cover almost all of the *V–I* plane region. The *V–I* planes obtained from the experimental platforms of the resonant converters are shown in Fig. 21. In order to draw the planes, the platforms have been tested under different output voltage and output current conditions. In each plane, there are different limitations on the boundaries, including current, voltage, and power, and each point in the boundary indicates one experimental test. The *V–I* plane obtained from the *LLC* resonant converter platform is shown in Fig. 21(a). Due to the effect of output diodes junction capacitances in no-load conditions, the output voltage increases for switching frequency higher than $300\mathrm{kHz}$ [as indicated in Fig. 15(a)]. Note that the unobtainable area of the *LLC* resonant converter starts in the no-load boundary at $V_{\mathrm{out}} = 72\mathrm{VDC}$. In order to decrease the output voltage to less than $72\mathrm{VDC}$, the output current should be increased from zero. Finally, in the minimum desired output voltage $V_{\mathrm{out}} = 1\mathrm{VDC}$, the output current is equal to $3\mathrm{A}$. The red-dashed region indicates the unobtainable area of the *LLC* resonant converter. Fig. 21(b) proves that the multiresonant $L3C2$ resonant converter can cover almost all of the region in the *V–I* plane. According to this figure, the minimum output voltage in no-load conditions occurs at $V_{\mathrm{out}} = 16\mathrm{VDC}$, and the area obtained by the proposed resonant converter is significantly extended in comparison with the *LLC V–I* plane. Fig. 21(b) demonstrates that the proposed $L3C2$ resonant converter is capable of covering the battery *V–I* plane, regulating the output voltage from near zero to 1.5 times nominal voltage in different load, and can be employed as a battery charger without using burst mode operation. Note that the topology can be employed for high-power applications and fast charging, beyond the $950\,\mathrm{W}$ example by using a full-bridge input inverter. The switching frequency during bulk charging is expected to be between $129–166\mathrm{kHz}$, according to the *V–I* plane depicted in Fig. 21(b). As indicated in the figure, the maximum power limit can provide maximum energy transfer to the batteries while maintaining moderate switching frequency.

IX. CONCLUSION

This paper introduced the multiresonant $L3C2$ resonant topology as a power converter that can regulate the output voltage in a wide range, from near zero voltage, zero current to the maximum output power, without using burst mode operation. The complete analysis of the resonant converter along with mathematical equations were presented. The equations were able to precisely predict the behavior of the converter. Due to wide output voltage regulation, the proposed resonant converter can respond to charge algorithms of different kind of batteries, such as Lead-acid and Li-Ion and is a good candidate for use as a charger in EVs. The main advantage of the proposed resonant converter is its ability to revitalize dead batteries in CCM. The low-ripple output voltage enhances the quality of the charging current in the recovery region, thereby increasing the life cycle of the battery. Also, soft switching of the MOSFETs and output rectifier diodes provide high efficiency, and the capability of working in high-switching frequency without any limitation. The simulation and experimental results obtained from a $96\text{-VDC}, 950\text{-W}$ power platform verify the theoretical analysis and the performance of the proposed converter in terms of coverage in the *V–I* plane.

REFERENCES

[1] M. Yilmaz and P. Krein, "Review of battery charger topologies, charging power levels, and infrastructure for plug-in electric and hybrid vehicles," *IEEE Trans. Power Electron.*, vol. 28, no. 5, pp. 2151–2169, May 2013.

[2] S. Barcellona, F. Ciccarelli, D. Iannuzzi, and L. Piegari, "Modeling and parameter identification of lithium-Ion capacitor modules," *IEEE Trans. Sustainable Energy*, vol. 5, no. 3, pp. 785–794, Jul. 2014.

[3] A. Nourai, B. P. Martin, and D. R. Fitchett, "Testing the limits [electricity storage technologies]," *IEEE Power Energy Mag.*, vol. 3, no. 2, pp. 40–46, Mar./Apr. 2005.

[4] M. Bhatt, W. G. Hurley, and W. H. Wolfle, "A new approach to intermittent charging of valve-regulated lead acid batteries in standby applications," *IEEE Trans. Ind. Electron.*, vol. 52, no. 5, pp. 1337–1342, Oct. 2005.

[5] M. C. Wehrey, "What's new with hybrid electric vehicles," *IEEE Power Energy Mag.*, vol. 2, no. 6, pp. 34–39, Nov./Dec. 2004.

[6] M. Pahlevaninezhad, P. Das, J. Drobnik, P. Jain, and A. Bakhshai, "A novel ZVZCS full-bridge DC/DC converter used for electric vehicles," *IEEE Trans. Power Electron.*, vol. 27, no. 6, pp. 12752–2769, Jun. 2012.

[7] F. Musavi, M. Craciun, D. Gautam, W. Eberle, and W. Dunford, "An LLC resonant DC-DC converter for wide output voltage range battery charging applications," *IEEE Trans. Power Electron.*, vol. 28, no. 12, pp. 5437–5445, Dec. 2013.

[8] F. Musavi, M. Craciun, M. Edington, W. Eberle, and W. Dunford "Practical design considerations for a LLC multi-resonant DC-DC converter in battery charging applications," in *Proc. Appl. Power Electron. Conf. Expo.*, 2012, pp. 2596–2602.

[9] F. Musavi, M. Craciun, D. Gautam, M. Edington, W. Eberle, and W. Dunford, "Control strategies for a LLC multi-resonant DC-DC converter in battery charging applications," in *Proc. Appl. Power Electron. Conf. Expo.*, 2013, pp. 1803–1813.

[10] B. Wang, X. Xin, S. Wu, H. Wu, J. Ying, "Analysis and implementation of LLC burst mode for light load efficiency improvement," in *Proc. Appl. Power Electron. Conf. Expo.*, 2009, pp. 58–64.

[11] R. W. Erickson and D. Maksimovic, *Fundamentals of Power Electronics.*, 2nd ed. Norwell, MA, USA: Kluwer, 2001.

[12] D. Gautam, F. Musavi, W. Eberle, and W. Dunford, "A zero-voltage switching full-bridge DC-DC converter with capacitive output filter for plug-in hybrid electric vehicle battery charging," *IEEE Trans. Power Electron.*, vol. 28, no. 12, pp. 5728–5735, Dec. 2013.

[13] B. Gu, C. Lin, B. Chen, J. Dominic, and J. Lai, "Zero-voltage-switching PWM resonant full-bridge converter with minimized circulating losses

and minimal voltage stresses of bridge rectifiers for electric vehicle battery chargers,” *IEEE Trans. Power Electron.*, vol. 28, no. 10, pp. 4657–4667, Oct. 2013.

[14] D. Gautam, F. Musavi, M. Edington, W. Eberle, and W. Dunford, “An automotive onboard 3.3-kW battery charger for PHEV application,” *IEEE Trans. Veh. Technol.*, vol. 61, no. 8, pp. 3466–3474, Oct. 2012.

[15] M. Pahlevaninezhad, S. Eren, P. Jain, and A. Bakhshai, “Self-sustained oscillating control technique for current-driven full-bridge DC/DC converter,” *IEEE Trans. Power Electron.*, vol. 28, no. 11, pp. 5293–5310, Nov. 2013.

[16] T. Mishima, K. Akamatsu, and M. Nakaoka, “A high frequency-link secondary-side phase-shifted full-range soft-switching PWM DC-DC converter with ZCS active rectifier for EV battery chargers,” *IEEE Trans. Power Electron.*, vol. 28, no. 12, pp. 5758–5773, Dec. 2013.

[17] M. K. Kazimierczuk and D. Czarkowski, *Resonant Power Converters*. New York, NY, USA: Wiley, 1995.

[18] R. L. Steigerwald, “A comparison of half-bridge resonant converter topologies,” *IEEE Trans. Power Electron.*, vol. 3, no. 2, pp. 174–182, Apr. 1988.

[19] C. Chang, E. Chang, and H. Cheng, “A high-efficiency solar array simulator implemented by an LLC resonant DC-DC converter,” *IEEE Trans. Power Electron.*, vol. 28, no. 6, pp. 3039–3046, Jun. 2013.

[20] H. Choi, “Analysis and design of LLC resonant converter with integrated transformer,” in *Proc. Appl. Power Electron. Conf. Expo.*, 2007, pp. 1630–1635.

[21] H. Hu, X. Fang, F. Chen, Z. Shen, and I. Batarseh, “A Modified high-efficiency LLC converter with two transformers for wide input-voltage range applications,” *IEEE Trans. Power Electron.*, vol. 28, no. 4, pp. 1946–1960, Apr. 2013.

[22] D. Kim, C. Kim, and G. Moon, “High-efficiency slim adapter with low-profile transformer structure,” *IEEE Trans. Ind. Electron.*, vol. 59, no. 9, pp. 3445–3449, Sep. 2012.

[23] H. Choi and FPS Application Group, *Half-Bridge LLC Resonant Converter Design Using FSFR-Series Fairchild Power Switch*, Fairchild Semiconductor Corporation, San Jose, CA, USA, Rev. 1.0.0 10/9/07, 2007.

[24] B. Lee, M. Kim, C. Kim, K. Park, and G. Moon, “Analysis of LLC resonant converter considering effects of parasitic components,” in *Proc. Telecommun. Energy Conf.*, 2009, pp. 1–5.

[25] I. Batarseh, “Resonant converter topologies with three and four energy storage elements,” *IEEE Trans. Power Electron.*, vol. 9, no. 1, pp. 64–73, Jan. 1994.

[26] C. P. Dick, *Multi-Resonant Converters as Photovoltaic Module-Integrated Maximum Power Point Tracker*. Maastricht, Germany: Shaker, 2010.

[27] C. P. Dick, F. K. Titiz, and R. W. Doncker, “A high-efficient LLCC series-parallel resonant converter,” in *Proc. Appl. Power Electron. Conf. Expo.*, 2010, pp. 696–701.

[28] P. K. Jain and M. C. Tanju, “Unity power factor resonant AC/DC converter for high-frequency space power distribution system,” *IEEE Trans. Power Electron.*, vol. 12, no. 2, pp. 325–331, Mar. 1997.

[29] N. Shafiei, M. Pahlevaninezhad, H. Farzanehfard, and S. Motahari, “Analysis and implementation of a fixed-frequency LCLC resonant converter with capacitive output filter,” *IEEE Trans. Ind. Electron.*, vol. 58, no. 10, pp. 4773–4782, Oct. 2011.

[30] Z. Ye, P. K. Jain, and P. C. Sen, “A two-stage resonant inverter with control of the phase angle and magnitude of the output voltage,” *IEEE Trans. Ind. Electron.*, vol. 54, no. 5, pp. 2797–2812, Oct. 2007.

[31] Z. Ye, J. C. W. Lam, P. K. Jain, and P. C. Sen, “A robust one-cycle controlled full-bridge series–parallel resonant inverter for a high-frequency AC (HFAC) distribution system,” *IEEE Trans. Power Electron.*, vol. 22, no. 6, pp. 2331–2343, Nov. 2007.

[32] Y. A. Ang, C. M. Bingham, M. P. Foster, D. A. Stone, and D. Howe, “Design oriented analysis of fourth-order LCLC converters with capacitive output filter,” *IET Power Electron.*, vol. 152, no. 2, pp. 310–322, 2005.

[33] D. Bortis , J. Biela , G. Ortiz and J. W. Kolar, “Design procedure for compact pulse transformers with rectangular pulse shape and fast rise times, *IEEE Trans. Dielectric Electr. Insul.*, vol. 18, no. 4, pp. 1171–1180, Aug. 2011.

[34] W. Flanagan, Handbook of Transformer Design and Applications, 2nd ed. New York, NY, USA: McGraw-Hill, 1992.

[35] N. Shafiei, M. Pahlevaninezhad, H. Farzanehfard, A Bakhshai and P. Jain, “Analysis of a fifth-order resonant converter for high-voltage DC power supplies, ”*IEEE Trans. Power Electron.*, vol. 28, no. 1, pp. 85–100, Jan. 2013.

[36] K. Cho, Y. Kim I. Cho, and G. Moon, “Transformer integrated with additional resonant inductor for phase-shift full-bridge converter with primary clamping diodes, ”*IEEE Trans. Power Electron.*, vol. 27, no. 5, pp. 2405–2414, May 2012.

[37] C. Bingham, Y. Ang, M. Foster, and D. Stone, “Analysis and control of dual-output LCLC resonant converters with significant leakage inductance, ”*IEEE Trans. Power Electron.*, vol. 23, no. 4, pp. 1724–1732, Jul. 2008.

[38] D. Wang and Y. Liu, “A zero-crossing noise filter for driving synchronous rectifiers of LLC resonant converter, ”*IEEE Trans. Power Electron.*, vol. 29, no. 4, pp. 1953–1965, Apr. 2014.

[39] D. C. Montgomery, *Design and Analysis of Experiments*. New York, NY, USA: Wiley, 2001.

[40] S. R. Cove, M. Ordonez, F. Luchino, and J. E. Quaicoe, “Applying response surface methodology to small planar transformer winding design, ”*IEEE Trans. Ind. Electron.*, vol. 60, no. 2, pp. 483–493, Feb. 2013.

Navid Shafiei (S’11) was born in Isfahan, Iran. He received the B.S. degree in electrical engineering from Kashan University, Kashan, Iran, in 2005, and the M.S. degree in electrical engineering from Islamic Azad University, Najafabad, Iran, in 2011. He is currently working toward the Ph.D. degree at the University of British Columbia, Vancouver, BC, Canada.

He was a Technical Designer in the Information and Communication Technology Institute, Isfahan University of Technology, Isfahan, Iran, from 2005 to 2013, where he was involved in design and implementation of resonant converters. His current research interests include resonant converters and their application in pure electric vehicles.

Martin Ordonez (S’02–M’09) was born in Neuquen, Argentina. He received the Ing. degree in electronics engineering from the National Technological University, Cordoba, Argentina, in 2003, and the M.Eng. and Ph.D. degrees in electrical engineering from the Memorial University of Newfoundland (MUN), St. Johns, NL, Canada, in 2006 and 2009, respectively.

He is currently an Assistant Professor with the Department of Electrical and Computer Engineering, University of British Columbia, Vancouver, BC, Canada. He is also a Canada Research Chair in Power Converters for Renewable Energy Systems, as well as an Adjunct Professor with Simon Fraser University, Burnaby, BC, Canada, and MUN. His industrial experience in power conversion includes research and development at Xantrex Technology Inc./Elgar Electronics Corp. (now AMETEK Programmable Power in San Diego, CA, USA), Deep-Ing Electronica de Potencia (Rosario, Argentina), and TRV Dispositivos (Cordoba, Argentina). With the support of industrial funds and the Natural Sciences and Engineering Research Council, he has contributed to more than 60 publications and R&D reports.

Dr. Ordonez is an Associate Editor of the IEEE Transactions on Power Electronics, serves on several IEEE committees, and reviews widely for IEEE/IET journals and international conferences. He received the David Dunsiger Award for Excellence in the Faculty of Engineering and Applied Science (2009) and the Chancellors Graduate Award/Birks Graduate Medal (2006), and became a Fellow of the School of Graduate Studies, MUN.